

ON INCLUSION OF TIME-VARYING SOURCE IN NUMERICAL APPROXIMATION TO ACOUSTIC WAVE EQUATION AND A NEGLECTED LIMITATION

ASHKAN JAVAHERIAN

*School of Electrical and Computer Engineering, College of Engineering, University of Tehran,
Tehran, Iran.*

*Department of Medical Physics and Biomedical Engineering, University College London, London,
UK, WC1E 6BT.*

ABSTRACT

Acoustic wave equation seeks to represent wavefield in terms of a radiation source which possesses finite energy over space and time. The wavefield may be represented over a surface bounding the source, and calculated by solving an associated boundary-value problem via imposing conditions on the boundary of a chosen solution space. This manuscript aims to study approaches for obtaining unique solution to acoustic wave equation in terms of either a volumetric radiation source s , or surface source. For the latter, the wavefield is described using a Kirchhoff-Helmholtz or Rayleigh-Sommerfeld integral over the surface. Using a monopole version of these integral formulae, a singlet surface source is defined in terms of minus normal pressure derivative $-(\partial/\partial\mathbf{n})p$ or its equivalent $\rho_0\partial u^n/\partial t$. Here, p is the pressure, ρ_0 is the ambient density, and $u^n = \mathbf{u} \cdot \mathbf{n}$ is the normal velocity with \mathbf{n} a unit vector outwardly normal to the surface. Using a dipole variant of these surface integral formulae, the surface source is defined as a doublet source in terms of pressure p . It will be shown that an interior-field dipole variant of these integral formulae represents the back-projected field from observations of the wavefield over a surface. The key step for numerically approximating all these derived analytical formulae is inclusion of source, and will be studied in this manuscript carefully. It will be shown that a numerical approximation of a dipole version of these surface integral formulae has a limitation for including obliquity factors or their equivalent solid angles, especially for describing a back-projected field from observations over a measurement surface.

1. INTRODUCTION

Acoustic wave equation is one of the most important partial differential equations (PDEs) in mechanics [1, 2, 3, 4, 5, 6, 7, 8], and has broad ranges of applications [9, 10, 11, 12, 13, 14, 15, 16, 17, 18, 19, 20, 21, 22]. The forcing term in the right-hand-side of this second-order PDE can be assumed time instant or time-varying. For biomedical applications, one important example for formation of time-instant acoustic sources is photo-acoustic (PA) effect, the process of absorption of optical energy, its conversion to heat and generation of local acoustic pressures via therm-elastic expansion. Because the PA effect, which leads to local rises in pressure, occurs in a time few orders of magnitude shorter than the time for propagation of acoustic waves, the acoustic source is assumed time-instant

E-mail address: ajavaherian83@gmail.com.

Date: February 2024.

[23, 24, 25, 26, 27, 28, 29, 30, 31, 32, 33, 34, 35, 36, 37, 38, 39, 40, 41, 42, 43]. For time-varying source, also known as *radiation source*, an important example is radiation from vibrating sources, e.g., piezoelectric transducers [44]. Modelling time-varying sources has received growing attention for biomedical applications, for example for back-projection step in photoacoustic tomography [23, 28, 30], forward propagation and back-projection steps in quantitative ultrasound tomography using full-wave inversion approaches [44, 45, 46, 47, 48, 49, 50, 51, 52, 53, 54, 55, 56, 57, 58, 59, 60], or for treatment planning using focused ultrasound, which is an emerging technology for treatment of medical disorders via targeting deep tissues by ultrasonic energy [61, 62, 63, 64, 65, 66, 67]. For the latter, an accurate solution to the wave equation is very important because of safety reasons [68].

The solution to the wave equation is typically nonunique. Therefore, Cauchy initial conditions in terms of the wavefield and its time derivative at time origin are enforced for obtaining unique solution. These initial conditions establish a causal relation between solution wavefield and source, i.e., the solution wavefield vanishes prior to the time the source starts radiating. Therefore, solving the wave equation can be expressed as uniquely representing the propagated wavefield in terms of the radiation source (forcing term) via applying the causality conditions. Let $d \in \{2, 3\}$ be the number of dimensions of the medium. The radiation source s is defined over a finite d -dimensional space (volume for $d = 3$) and time and is assumed to possess finite energy, i.e., it is square-integrable over space and time. Furthermore, the wavefield may be represented in terms of integral formulae *Kirchhoff-Helmholtz* or *Rayleigh-sommerfeld*, in which the integration is taken over a surface bounding the source. The former is used for surface sources with arbitrary geometries, for example sphere or cylinder, and the latter is used for planar surface sources. Typically, the integrand appearing in these formulae is a function of pressure and its normal derivative over the surface bounding the source. However, because the wave equation establishes a dependence between these quantities over the chosen surface, the solution wavefield will be well-determined, if the associated integral formula over the surface bounding the source is defined in terms of only one of these quantities, i.e., pressure or its normal derivative. Therefore, to obtain a unique solution using theses surface integral formulae, in addition to Cauchy conditions satisfying the causality, conditions must be imposed on the boundary of a chosen solution space. The choice for the solution space and the conditions imposed on its boundary depend on the physics of the problem. Accordingly, the source may be defined as a $d - 1$ dimensional (surface for $d = 3$) singlet source in terms of minus normal pressure derivative $-(\partial/\partial\mathbf{n})p$ or its equivalent $\rho_0\partial u^{\mathbf{n}}/\partial t$, where ρ_0 is the ambient density and $u^{\mathbf{n}} = \mathbf{u} \cdot \mathbf{n}$ is the normal velocity with \mathbf{n} a unit vector outwardly normal to the surface. This representation is equivalent to a *monopole* variant of these integral formulae, and assumes a vibrating piston surrounded by a soft baffle, for which the pressure p over the surface of the piston vanishes. Using an assumption of a rigid baffle, the normal pressure derivative $-(\partial/\partial\mathbf{n})p$ over the surface vanishes, and the wavefield is defined in terms of a doublet surface source p . The latter representation is equivalent to a *dipole* variant of these integral formulae. Correspondingly, it will be shown that a *back-projected* field is represented using an *Interior-field Kirchhoff-Helmholtz* integral formula in terms of a *time-reversed* variant of a wavefield measured over a surface with arbitrary geometries (for example sphere or cylinder), or using an *Interior-field Rayleigh-Sommerfeld* integral formula in terms of a wavefield measured over a planar surface.

It will be shown that a numerical approximation of the wave equation is equivalent to representing the propagated wavefield as a weighted superposition of actions of a causal (or diverging) Green's function on a radiation or singlet source defined on a number of points sampled over a d or $d - 1$ dimensional space of support of the source, respectively, and over finite time of radiation of source. The weighting parameter associated with each sampled point is proportional to the contribution of

the volume or surface of the source to that sampled point. The key step for an accurate numerical approximation of the wave equation in the time domain is modelling the mass source. It will be shown that a numerical approximation of a doublet surface source using a full-wave method has a limitation for accounting for *Obliquity factor* or its equivalent *solid angle*, the angle an elemental area on the surface of source is seen by any arbitrary point in the solution space. This problem is more dominant for approximating a *back-projected* wavefield, which is radiated by a *time-reversed* variant of the wavefield measured on receivers placed on the whole measurement surface simultaneously.

Section 2 introduces the wave equation in the time domain. This section will explain how a unique solution to the wave equation can be obtained using homogeneous Cauchy conditions which establish a causal relation between solution wavefield and radiation source. A *primary* solution to the wave equation, which describes the propagated wavefield in terms of a d -dimensional (volumetric for $d = 3$) radiation source, will be described, and a *Kirchhoff-Helmholtz* solution to the wave equation, which solves the wavefield in terms of a surface source, will be derived. It will be explained how the boundary conditions of *Dirichlet* or *Neumann* types can be imposed for obtaining a unique solution for an arising over-determined formula describing the *Kirchhoff-Helmholtz* solution. Section 3 describes the *primary* and *Kirchhoff-Helmholtz* solutions to the wave equation in the frequency domain. Furthermore, a *Rayleigh-sommerfeld* solution to the wave equation will be explained for cases in which the surface source is mounted on a flat plane. Section 4 summarises the time-domain variant of surface integral formulae. Section 5 describes how the derived time-domain analytical formulae can be numerically approximated on a regular grid discretised in space and time. Specifically, this section describes how the mass source is defined, discretised and is given as an input to numerical systems for solving the wave equation in the time domain. In section 6, the time-domain analytic formulae will be compared to their numerical approximation on a regular grid for a source defined on a single point in space. Section 6 contains a brief discussion about the explained approaches and the obtained numerical results.

2. WAVE EQUATION IN THE TIME DOMAIN

This section considers the propagation of acoustic waves from a real-valued space and time-varying source in an infinite, isotropic and homogeneous medium in free space. Let $\mathbf{x} = (x^1, \dots, x^d)$ denote a spatial position in \mathbb{R}^d with $d \in \{2, 3\}$ the number of dimensions. Here, the analysis is done for $d = 3$, but it also holds for $d = 2$ by changing the volumes to surfaces, and surfaces to lines. (A line source produces acoustic waves which propagate as cylindrical waves in a 3D medium, and is equivalent to an omnidirectional point source in a 2D medium.) The real-valued wavefield satisfies the inhomogeneous wave equation, which is in the form

$$\frac{1}{c^2} \frac{\partial^2}{\partial t^2} p(\mathbf{x}, t) - \rho_0 \nabla \cdot \frac{1}{\rho_0} \nabla p(\mathbf{x}, t) = s(\mathbf{x}, t). \quad (1)$$

Here, the term in the right-hand-side is the forcing term $s(\mathbf{x}, t)$, also known as *radiation source*, and is assumed compactly supported in $\chi_s = \{\mathbf{x} \in \nu_s, t \in [0, T_s]\}$, where ν_s is a d -dimensional space (volume for $d = 3$), and $[0, T_s]$ is radiation time of the source. The source has units $\text{kgm}^{-d}\text{s}^{-2}$. It is assumed that the source s is square-integrable in χ_s . In addition, c is velocity of wave propagation in medium and has units ms^{-1} , and ρ_0 is ambient density of medium and has units kgm^{-d} . Furthermore, p denotes the pressure wavefield, which is the unknown parameter of the wave equation, and has units $\text{kgm}^{2-d}\text{s}^{-2}$ (or Pascal). By assuming constant values for ρ_0 , the wave equation (1) is

reduced to its canonical form

$$\left[\frac{1}{c^2} \frac{\partial^2}{\partial t^2} - \nabla^2\right] p(\mathbf{x}, t) = s(\mathbf{x}, t). \quad (2)$$

2.1. Cauchy conditions for unique solution. The solution to the wave equation is nonunique. A unique solution is obtained by confining the wavefield to a particular solution which is causally related to the source, i.e., a wavefield p which vanishes prior to the time $t = 0$, the initial time of radiation of source. By imposing the Cauchy conditions

$$p_+(\mathbf{x}, t)|_{t=0} = 0, \quad \frac{\partial}{\partial t} p_+(\mathbf{x}, t)|_{t=0} = 0, \quad (3)$$

a causal solution to the wave equation (2) is obtained, where the subscript $+$ stands for the causality. The problem of solving the inhomogeneous wave equation (2), together with the causality conditions, i.e., Cauchy conditions (3), is called *radiation* problem. Note that by setting the forcing term s zero, and relaxing the Cauchy conditions (3) to arbitrary and inhomogeneous fields at $t = 0$, the wave equation (2) will be an *initial-value* problem, which arises for example in photoacoustic tomography. The focus of this manuscript is on analytic and numerical solutions to the *radiation* problem.

2.2. Green's function solution to the wave equation. Consider the wave equation (2) as a radiation problem for a particular choice $s(\mathbf{x}, t) = \delta(\mathbf{x} - \mathbf{x}')\delta(t - t')$, where $\delta(\cdot)$ is the Dirac delta function, and \mathbf{x}' and t' are free parameters in space and time domains, respectively. In an infinite free space, a Green's function solution to the wave equation then satisfies

$$\left[\frac{1}{c^2} \frac{\partial^2}{\partial t^2} - \nabla^2\right] g(\mathbf{x} - \mathbf{x}', t - t') = \delta(\mathbf{x} - \mathbf{x}')\delta(t - t'). \quad (4)$$

For brevity, from now on, the Green's function will be written in the form

$$g(\mathbf{x}_\partial, t_\partial) = g(\mathbf{x} - \mathbf{x}', t - t'), \quad (5)$$

where $\mathbf{x}_\partial = \mathbf{x} - \mathbf{x}'$ and $t_\partial = t - t'$. Similar to the wave equation (2), a unique solution to Eq. (4) is satisfied by assuming a causality condition for the Green's function, i.e., $g_+(\mathbf{x}_\partial, t_\partial) = 0$ for $t_\partial < 0$. For $d = 3$, a causal Green's function satisfies

$$g_+(\mathbf{x}_\partial, t_\partial) = \frac{1}{4\pi} \frac{\delta(t_\partial - \frac{x_\partial}{c})}{x_\partial}. \quad (6)$$

where $x_\partial = |\mathbf{x}_\partial|$. The reader is referred to Appendix A for derivation of the causal (or retarded) Green's function (6). Let us now rewrite the wave equations (2) and (4) in the forms

$$\left[\frac{1}{c^2} \frac{\partial^2}{\partial t'^2} - \nabla_{\mathbf{x}'}^2\right] p_+(\mathbf{x}', t') = s(\mathbf{x}', t'), \quad (7)$$

and

$$\left[\frac{1}{c^2} \frac{\partial^2}{\partial t'^2} - \nabla_{\mathbf{x}'}^2\right] g(\mathbf{x} - \mathbf{x}', t - t') = \delta(\mathbf{x} - \mathbf{x}')\delta(t - t'), \quad (8)$$

respectively, where \mathbf{x} and t are fixed parameters in a closed set $\chi = \{\mathbf{x} \in \nu, t \in [t_0, t_1]\}$ within which the solution is sought. Now, multiplying (7) by $g(\mathbf{x}_\partial, t_\partial)$ and (8) by $p_+(\mathbf{x}', t')$, and then subtracting the modified (8) from the modified (7), yield [70]

$$(\nabla^2 g)p_+ - g\nabla^2 p_+ - \frac{1}{c^2} \left[\left(\frac{\partial^2}{\partial t'^2} g \right) p_+ - g \frac{\partial^2}{\partial t'^2} p_+ \right] = gs - \delta(\mathbf{x}_\partial)\delta(t_\partial) p_+, \quad (9)$$

where the dependence on space and time has been neglected for brevity. Now, integrating the left side of Eq. (9) over the chosen spatio-temporal solution set χ gives

$$\int_{t_0}^{t_1} dt' \int_{\nu} d\mathbf{x}' \nabla \cdot [(\nabla g)p_+ - g\nabla p_+] - \frac{1}{c^2} \int_{t_0}^{t_1} dt' \int_{\nu} d\mathbf{x}' \frac{\partial}{\partial t'} [(\frac{\partial}{\partial t'} g)p_+ - g\frac{\partial}{\partial t'} p_+]. \quad (10)$$

Now, applying the well-known Green's theorem to the first term in (10), taking the temporal integral of the second term in (10), and then taking the integral of the right-hand side in (9) over the solution set χ , give [70]

$$\begin{aligned} & \int_{t_0}^{t_1} dt' \int_{\partial\nu} dS' [(\frac{\partial}{\partial \mathbf{n}'} g)p_+ - g\frac{\partial}{\partial \mathbf{n}'} p_+] - \frac{1}{c^2} \int_{\nu} d\mathbf{x}' [(\frac{\partial}{\partial t'} g)p_+ - g\frac{\partial}{\partial t'} p_+] \Big|_{t_0}^{t_1} = \\ & \int_{t_0}^{t_1} dt' \int_{\nu} d\mathbf{x}' g s - \begin{cases} p_+, & \text{if } \mathbf{x} \in \nu, t \in [t_0, t_1] \\ 0, & \text{otherwise,} \end{cases} \end{aligned} \quad (11)$$

where \mathbf{n}' is an outward unit vector normal to the surface $\partial\nu$.

2.2.1. Primary solution. A primary solution for all space and all time can be obtained by choosing g to be the causal Green's function g_+ , and enlarging the spatio-temporal set χ to infinity. Accordingly, the limits $\nu \rightarrow \infty$, $t_0 \rightarrow -\infty$ and $t_1 \rightarrow \infty$ are taken. Now, for the second term in the left-hand-side of Eq. (11), by the assumption of causality, p_+ vanishes at $t = -\infty$ and g vanishes for the time $t = +\infty$, and the second term will thus drop. In addition, considering that a causal Green's function gives $g(\mathbf{x}_\partial, t_\partial) = 0$ unless $x_\partial = ct_\partial$, the contribution from surface $\partial\nu$ with infinite radius vanishes for any finite and arbitrarily large value for t_1 [70]. Therefore, the left-hand-side of Eq. (11) vanishes as well, and therefore, the primary solution for p_+ at any pair of \mathbf{x} and t which lie in the set χ satisfies

$$p_+(\mathbf{x}, t) = \int_0^{T_s} dt' \int_{\nu_s} d\mathbf{x}' g_+(\mathbf{x}_\partial, t_\partial) s(\mathbf{x}', t'). \quad (12)$$

Therefore, the *Primary* formula (12) represents the solution wavefield in terms of the radiation source s , which is the forcing term in the right-hand-side of the wave equation. Considering the infinity assumptions used for the set χ , this solution holds over all space and all time.

2.2.2. Exterior-field Kirchhoff-Helmholtz solution. This section describes the *Kirchhoff-Helmholtz solution* to the wave equation. The corresponding theory was developed in optics for describing light diffraction from a small aperture mounted in a dark screen, and was then extended to acoustics for describing a vibrating piston surrounded in a baffle. The Equation (12), which gives a primary solution, directly maps the forcing term s to the wavefield solution p_+ , and is based on an integration of source s over its volumetric support. However, for many problems, the source is quantified over an external surface. Correspondingly, a more practical formula can be derived based on assuming ν a finite volume which contains the source volume ν_s . It is assumed that the volume ν has a closed boundary $\partial\nu$, and the space in which the solution is sought is confined to the volume lying outside $\partial\nu$ [70]. Now, considering the assumption of a causal solution to the wave equation (7) over a time $[t_0, t_1]$ with $t_0 \rightarrow -\infty$ and $t_1 \rightarrow +\infty$ and using an assumption of causality for the Green's function solution in (8), a solution is sought in the volume ν^C , which is bounded by the closed surface $\partial\nu$ and the closed boundary of a sphere with a radius of infinity. The procedure is the same as in section 2.2.1, except the integral in Eq. (11) is taken over ν^C , instead of ν . Accordingly, the second term in the left-hand-side of Eq. (11) vanishes because of causality of p_+ and g_+ , the same as in section 2.2.1. For the first term in Eq. (11), the contribution of the surface with infinity radius vanishes,

as discussed in section 2.2.1. Therefore, the field p_+ which resides in the solution space ν^C , satisfies [70]

$$\int_{-\infty}^{\infty} dt' \int_{\partial\nu} dS' \left[\left(\frac{\partial}{\partial \mathbf{n}'} g_+ \right) p_+ - g_+ \frac{\partial}{\partial \mathbf{n}'} p_+ \right] = \begin{cases} p_+(\mathbf{x}, t), & \mathbf{x} \in \nu^C \\ 0, & \mathbf{x} \in \nu \end{cases} \quad (13)$$

where \mathbf{n}' is a unit vector normal to the surface $\partial\nu$ and directed outward from the interior volume ν to the exterior volume ν^C in which the solution is sought. In Eq. (13), the formula for the exterior volume is called *first Helmholtz identity*, and describes a solution wavefield outside the chosen surface $\partial\nu$ bounding the source volume ν_s as a function of the field and its outward-directed normal derivative over that surface. The formula for the internal volume is called *second Helmholtz identity*, and is a homogeneous integral equation, which establishes a dependence between the field and its normal derivative over the surface $\partial\nu$. Because of the dependence established by the *second Helmholtz identity* over the surface $\partial\nu$, the *first Helmholtz identity* is an over-determined problem. Therefore, boundary conditions must be imposed to make this formula well-determined. This requires that the integrand in the *Kirchhoff-Helmholtz* formula (13) be a function of only the wavefield, only its normal derivative, or a linear combination of both. These can be satisfied by imposing *Dirichlet*, *Neumann* or *Mixed* boundary conditions, respectively.

2.2.3. Interior-field Kirchhoff-Helmholtz solution. It was shown how the causal pressure field and its outwardly-directed normal derivative over a surface $\partial\nu$ which encompasses the source can be used to represent the field at points exterior to this surface. The solution to the *Exterior-field Kirchhoff-Helmholtz* integral is solution to a *forward* propagation problem. In this section, the solution to *back-projection* or *time-reversal* problem is described. For times larger than the turn-off time of the radiation source, T_s , the field in the interior region ν , which contains the source, satisfies the homogeneous (vanishing) Cauchy conditions and can thus be represented in terms of the field and its normal derivative over the surface $\partial\nu$ in the form of a boundary-value problem. In the formula (11), setting the space ν finite and encompassed by a closed boundary $\partial\nu$ and again taking the limits $t_0 \rightarrow -\infty$ and $t_1 \rightarrow +\infty$, give an integral formula in terms of an incoming-wave Green's function in the form

$$\int_{-\infty}^{\infty} dt' \int_{\partial\nu} dS' \left[g_- \frac{\partial}{\partial \mathbf{n}'} p_+ - \left(\frac{\partial}{\partial \mathbf{n}'} g_- \right) p_+ \right] = \begin{cases} p_+(\mathbf{x}, t), & \mathbf{x} \in \nu, t > T_s, \\ 0, & \mathbf{x} \in \nu^C, t > T_s, \end{cases} \quad (14)$$

where \mathbf{n}' is a unit normal vector directed outward of the interior volume ν into the exterior volume ν^C and g_- is an *anti-causal* (or *incoming-wave*) Green's function. In the formula (14), transformations $t \rightarrow -t$ and $t' \rightarrow -t'$, and replacing the outward unit normal vector \mathbf{n}' by an inward unit normal vector \mathbf{n}'_- from ν^C to ν , give

$$\phi(\mathbf{x}, -t) = \int_{-\infty}^{\infty} dt' \int_{\partial\nu} dS' \left[\left(\frac{\partial}{\partial \mathbf{n}'_-} g_+(\mathbf{x}_\partial, t_\partial) \right) p_+(\mathbf{x}', -t') - g_+(\mathbf{x}_\partial, t_\partial) \frac{\partial}{\partial \mathbf{n}'_-} p_+(\mathbf{x}', -t') \right], \quad (15)$$

which is termed *back-projected* field and satisfies $\phi(\mathbf{x}, -t) = p_+(\mathbf{x}, -t)$ for $t < -T_s$. The formula (15) implies that the *back-projected* field is radiated by time-reversed value fields within times t_∂ for $t < -T_s$. As discussed above, because the solution to the surface integral in the interior region is over-specified, the Green's functions satisfying homogeneous *Neumann* or *Dirichlet* boundary conditions are used for obtaining unique solutions. In practice, because the data is measured over a measurement surface in terms of the wavefield, a homogeneous *Dirichlet* boundary condition is applied for the *back-projection* (or *time-reversal* propagation).

3. WAVE EQUATION IN THE FREQUENCY DOMAIN

In this section, the wave equation is treated in the temporal frequency domain. Here, the temporal Fourier transform of a function or field and its inverse is defined by

$$F(\mathbf{x}, \omega) = \int_{-\infty}^{\infty} dt f(\mathbf{x}, t) e^{i\omega t}, \quad f(\mathbf{x}, t) = \frac{1}{2\pi} \int_{-\infty}^{\infty} d\omega F(\mathbf{x}, \omega) e^{-i\omega t}. \quad (16)$$

Taking a temporal Fourier transform of (4) gives the *Helmholtz* equation of the form

$$\left[\frac{\omega^2}{c^2} + \nabla^2 \right] G(\mathbf{x}_\partial, \omega) = -\delta(\mathbf{x}_\partial), \quad (17)$$

where $G(\mathbf{x}_\partial, \omega)$ is the frequency-domain Green's function, which relates to the time-domain Green's function through the pair of equations

$$G(\mathbf{x}_\partial, \omega) = \int_{-\infty}^{+\infty} dt_\partial g(\mathbf{x}_\partial, t_\partial) e^{i\omega t_\partial}, \quad g(\mathbf{x}_\partial, t_\partial) = \frac{1}{2\pi} \int_{-\infty}^{+\infty} d\omega G(\mathbf{x}_\partial, \omega) e^{-i\omega t_\partial}. \quad (18)$$

3.1. Causality condition and outgoing Green's function. Like Eq. (4), the solution to the inhomogeneous wave equation (17) is not unique, and therefore, constraints must be enforced to obtain a unique solution. It will be shown below that causality condition described for the time-domain wave equation results in a boundary condition at infinity in the temporal frequency domain. The associated Green's function can be derived from a spatio-temporal Fourier transform of the wave equation (17). (See Appendix A.) This approach yields

$$G_+(\mathbf{x}_\partial, \omega) = \frac{1}{4\pi} \frac{e^{ikx_\partial}}{x_\partial}, \quad (19)$$

where $x_\partial = |\mathbf{x}_\partial|$ and $k = \omega/c$ is the wavenumber. Here, the subscript $+$ indicates that the Green's function is outgoing. Substituting (19) into the inverse Fourier formula defined in the right equation in (18) gives

$$g_+(\mathbf{x}_\partial, t_\partial) = \frac{1}{2\pi} \int_{-\infty}^{\infty} dk \frac{1}{4\pi} \frac{e^{ik(x_\partial - ct_\partial)}}{x_\partial}. \quad (20)$$

Here, the Green's function is expressed as a superposition of time-harmonic waves with spherical surfaces of constant phase $x_\partial - ct_\partial$. These constant-phase surfaces are outgoing, because by initialising at $t_\partial = 0$ and increasing t_∂ , a constant phase requires that x_∂ increases proportionally, and that implies that a causal Green's function is *outgoing* or *diverging*.

Remark 1. An equivalent causal Green's function can be obtained for 2D media, where \mathbf{x} is now a position in a plane. Accordingly, an asymptotic expansion of the 2D Green's function in a homogeneous medium satisfies

$$G_+^{2D}(\mathbf{x}_\partial, \omega) = \frac{i}{4} H_0^+(kx_\partial) \approx \left[\frac{1}{8\pi kx_\partial} \right]^{1/2} e^{i(kx_\partial + \frac{\pi}{4})}, \quad kx_\partial \rightarrow \infty, \quad (21)$$

where kx_∂ is the accumulated phase.

3.2. Green's function solution to the wave equation. This section describes the solutions to the wave equation in the frequency domain. Like section 2.2, the wavefield solution will first be derived in terms of a volumetric radiation source s , and the obtained solution will then be extended to wavefield in terms of a source defined over an external surface which bounds a volumetric space ν_s representing the support of the radiation source s .

3.2.1. *Primary solution.* Below, a primary solution to the inhomogeneous wave equation in the frequency domain is described. Plugging the inverse Fourier transform (18) in the time-domain primary solution (12), and then applying the replacement

$$S(\mathbf{x}', \omega) = \int_0^{T_s} dt' e^{i\omega t'} s(\mathbf{x}', t'), \quad (22)$$

yield a frequency-domain primary solution, which is in the form

$$P_+(\mathbf{x}, \omega) = \int_{\nu_s} d\mathbf{x}' G_+(\mathbf{x}_\partial, \omega) S(\mathbf{x}', \omega), \quad (23)$$

where $t_\partial = t - t'$ has been used.

3.2.2. *Exterior-field Kirchhoff-Helmholtz solution.* Here, the *Exterior-field* variant of the *Kirchhoff-Helmholtz* formula is defined in the frequency domain, and the frequency-domain version of the *Interior-field* variant is left for the readers. (See section 2.2.3.) Accordingly, the frequency-domain version of the *Exterior-field Kirchhoff-Helmholtz* formula (13) gives [70]

$$\int_{\partial\nu} dS' \left[\left(\frac{\partial}{\partial \mathbf{n}'} G_+(\mathbf{x}_\partial, \omega) \right) P_+(\mathbf{x}', \omega) - G_+(\mathbf{x}_\partial, \omega) \frac{\partial}{\partial \mathbf{n}'} P_+(\mathbf{x}', \omega) \right] = \begin{cases} P_+(\mathbf{x}, \omega), & \mathbf{x} \in \nu^c \\ 0, & \mathbf{x} \in \nu, \end{cases} \quad (24)$$

where it is reminded that \mathbf{n}' is a unit vector and outwardly normal from the interior volume ν , which contains the source volume ν_s , to the exterior volume ν^c , which is the solution space. As discussed in section 2.2.2, the equation for $\mathbf{x} \in \nu^c$ is termed the *first Helmholtz identity*, and is an over-determined problem. The reason is that because the surface integral for $\mathbf{x} \in \nu$, known as the *second Helmholtz identity*, vanishes, a dependence is established between the field and its normal derivative over $\partial\nu$. Therefore, conditions must be imposed on the surface $\partial\nu$ to make the problem well-determined. Correspondingly, by imposing the *Neumann* or *Dirichlet* boundary conditions, the formula (24) is reduced to monopole formula

$$P_+^N(\mathbf{x}, \omega) = - \int_{\partial\nu} dS' G_+^N(\mathbf{x}_\partial, \omega) \frac{\partial}{\partial \mathbf{n}'} P_+(\mathbf{x}', \omega), \quad \frac{\partial}{\partial \mathbf{n}'} G_+^N(\mathbf{x}_\partial, \omega)|_{\mathbf{x}' \in \partial\nu} = 0 \quad (25)$$

and dipole formula

$$P_+^D(\mathbf{x}, \omega) = \int_{\partial\nu} dS' \left[\frac{\partial}{\partial \mathbf{n}'} G_+^D(\mathbf{x}_\partial, \omega) \right] P_+(\mathbf{x}', \omega), \quad G_+^D(\mathbf{x}_\partial, \omega)|_{\mathbf{x}' \in \partial\nu} = 0, \quad (26)$$

respectively. Here, $\mathbf{x} \in \nu^c$, and G_+^N and G_+^D are causal Green's functions satisfying the homogeneous *Neumann* and *Dirichlet* boundary conditions over $\partial\nu$, respectively.

3.2.3. *Exterior-field Rayleigh-Sommerfeld solution.* A common Green's approach for solving the boundary-value problem of the Helmholtz wave equation is the *Rayleigh-Sommerfeld* solution. Using this approach, the solution space is taken a half-space which is bounded by an infinite plane $\partial\nu$ and an infinite hemisphere. For simplicity, the bounding plane is assumed $x^3 = 0$, and the solution is sought in the half-space $x^3 > 0$. As discussed above, the associated *Kirchhoff-Helmholtz* integral formula is over-determined. To make this problem well-determined, the boundary conditions of the form *Dirichlet* or *Neumann* are imposed on the bounding plane, and the SRC condition is applied on the infinite surface. (See Appendix B.) A popular method for solving this boundary-value problem is *method of images* [70]. Accordingly, \mathbf{x} and \mathbf{x}' are used to denote the position of the general field and a point source in a 3D medium, and it is assumed that both lie in the half-space $\nu^+ = \{\mathbf{x} : x^3 > 0\}$. Using the notation $\mathbf{x}' = (x'^1, x'^2, x'^3)$, another mirror-image source point $\tilde{\mathbf{x}}' = (x'^1, x'^2, -x'^3)$ is introduced [70]. Accordingly, considering that \mathbf{x} and $\tilde{\mathbf{x}}'$ lie at different

sides of the plane, and therefore $\delta(\mathbf{x} - \tilde{\mathbf{x}}') = 0$, a Helmholtz equation with an augmented forcing term can be defined in the form

$$[k^2 + \nabla_{\mathbf{x}}^2] G_+^N(\mathbf{x} - \mathbf{x}', \omega) = -\delta(\mathbf{x} - \mathbf{x}') - \delta(\mathbf{x} - \tilde{\mathbf{x}}'), \quad (27)$$

where the Green's function G_+^N satisfies

$$G_+^N(\mathbf{x} - \mathbf{x}', \omega) = G_+(\mathbf{x} - \mathbf{x}', \omega) + G_+(\mathbf{x} - \tilde{\mathbf{x}}', \omega), \quad (28)$$

and also satisfies the SRC condition over the infinite surface. (See Appendix B.) For a point source \mathbf{x}' which tends to lie on the bounding plane $x^3 = 0$, $|\mathbf{x} - \tilde{\mathbf{x}}'| = |\mathbf{x} - \mathbf{x}'|$, and thus the Green's function in (28) satisfies

$$G_+^N(\mathbf{x}_{\mathfrak{d}}, \omega)|_{x^3=0} = 2G_+(\mathbf{x}_{\mathfrak{d}}, \omega)|_{x^3=0}, \quad \frac{\partial}{\partial \mathbf{n}'} G_+^N(\mathbf{x}_{\mathfrak{d}}, \omega)|_{x^3=0} = 0. \quad (29)$$

Now, plugging the Green's function G_+^N into the *Kirchhoff-Helmholtz* formula (24) yields the monopole formula

$$P_+^N(\mathbf{x}, \omega) = -a_p \int_{(\partial\nu=\{\mathbf{x}':x'^3=0\})} dS' G_+^N(\mathbf{x}_{\mathfrak{d}}, \omega) \frac{\partial}{\partial \mathbf{n}'} P_+(\mathbf{x}', \omega), \quad \frac{\partial}{\partial \mathbf{n}'} G_+^N(\mathbf{x}_{\mathfrak{d}}, \omega)|_{x^3=0} = 0, \quad (30)$$

where $a_p = 2$, and we remind that $\mathbf{x} \in \nu^+$ with ν^+ the half-space $\{\mathbf{x} : x^3 > 0\}$, and the integral has been taken over the surface $\partial\nu$, which is here set the plane $x^3 = 0$. Also, \mathbf{n}' is a unit vector normal to the plane $x^3 = 0$ and directed to the solution half-space ν^+ . In addition, it can be shown by some minor algebra that imposing a homogeneous *Dirichlet* boundary condition for the Green's function on this plane will give the dipole formula [70]

$$p_+^D(\mathbf{x}, \omega) = a_p \int_{(\partial\nu=\{\mathbf{x}':x'^3=0\})} dS' \left[\frac{\partial}{\partial \mathbf{n}'} g_+^D(\mathbf{x}_{\mathfrak{d}}, \omega) \right] p(\mathbf{x}', \omega), \quad g_+^D(\mathbf{x}_{\mathfrak{d}}, \omega)|_{x^3=0} = 0, \quad (31)$$

where $a_p = 2$.

4. GREEN'S FUNCTION SOLUTION IN THE TIME DOMAIN

This section describes the well-determined Green's function solutions to the wave equation in the time domain.

4.1. Monopole formula. The monopole formula is derived by an assumption of a piston vibrating in a soft baffle. For this case, it is assumed that the pressure over the surface of the piston vanishes. Correspondingly, using a causal Green's function g_+^N , which satisfies a homogeneous *Neumann* condition over the surface $\partial\nu$ bounding the source, the integral over that surface is defined in terms of the normal pressure derivative $-(\partial/\partial \mathbf{n}')p_+$, which is a *singlet* surface source. Accordingly, the monopole variants of *Kirchhoff-Helmholtz* or *Rayleigh-Sommerfeld* formulae in the time domain yield

$$p_+^N(\mathbf{x}, t) = -a_p \int_0^{T_s} dt' \int_{(\partial\nu=\{\mathbf{x}':x'^3=0\})} dS' g_+^N(\mathbf{x}_{\mathfrak{d}}, t_{\mathfrak{d}}) \frac{\partial}{\partial \mathbf{n}'} p(\mathbf{x}', t'), \quad \frac{\partial}{\partial \mathbf{n}'} g_+^N(\mathbf{x}_{\mathfrak{d}}, t_{\mathfrak{d}})|_{\partial\nu} = 0, \quad (32)$$

where for the *Exterior-field Kirchhoff-Helmholtz* solution, $\mathbf{x} \in \nu^{\mathcal{C}}$ and $a_p = 1$, and for the *Exterior-field Rayleigh-Sommerfeld* solution, $\mathbf{x} \in \nu^+$ and $a_p = 2$.

4.2. Dipole formula. The dipole formula is derived by an assumption of a rigid baffle, in which the normal pressure derivative over the surface of the vibrating piston vanishes. Therefore, using a causal Green's function g_+^D , which satisfies a homogeneous *Dirchilet* condition over $\partial\nu$, the surface integral is defined in terms of the pressure p_+ , which is a *doublet* surface source. Correspondingly, dipole variants of the *Kirchhoff-Helmholtz* or *Rayleigh-Sommerfeld* formulae give

$$\begin{aligned} p_+^D(\mathbf{x}, \omega) &= a_p \int_{\partial\nu} dS' [\mathbf{n}' \cdot \nabla_{\mathbf{x}'} g_+^D(\mathbf{x}_\partial, \omega)] p(\mathbf{x}', \omega), \\ &= a_p \int_{\partial\nu} dS' [\mathbf{n}' \cdot \frac{\mathbf{x}_\partial}{x_\partial}] g_+^D(\mathbf{x}_\partial, \omega) \left[-ik + \frac{1}{x_\partial} \right] p(\mathbf{x}', \omega), \quad g_+^D(\mathbf{x}_\partial, t_\partial)|_{\partial\nu} = 0, \end{aligned} \quad (33)$$

where we remind that $\mathbf{x}_\partial = \mathbf{x} - \mathbf{x}'$. Note that the second term in the bracket, $1/x_\partial$, is often included in ray-based methods, because it can be calculated for each ray separately and efficiently and acts as a ramp filter on low frequencies, which may not be useful for imaging. See [69] for an application for approximation of back-projected field from measurements over a surface in photoacoustic tomography. For full-wave approaches, an approximation of this term is not straightforward, because the integral formula is solved simultaneously for the whole surface of the source. Therefore, by using a *far-field* approximation $kx_\partial \gg 1$, which often holds, a time-domain variant of Eq. (33) yields

$$p_+^D(\mathbf{x}, t) \approx -a_p \int_0^{T_s} dt' \int_{\partial\nu} dS' [\mathbf{n}' \cdot \frac{\mathbf{x}_\partial}{x_\partial}] g_+^D(\mathbf{x}_\partial, t_\partial) \left[\frac{1}{c} \frac{\partial}{\partial t'} p(\mathbf{x}', t') \right], \quad g_+^D(\mathbf{x}_\partial, t_\partial)|_{\partial\nu} = 0, \quad (34)$$

where $\mathbf{n}' \cdot (\mathbf{x}_\partial/x_\partial)$ is the *obliquity factor*. Note that the integral formula (34) can be written in terms of a solid angle element $d\Omega_{\mathbf{x}}(S'(\mathbf{x}'))$, which is the angle an infinitesimal elemental area dS' corresponding to the point \mathbf{x}' on the surface can be seen from an arbitrary point \mathbf{x} , and is defined in the form

$$d\Omega_{\mathbf{x}}(S'(\mathbf{x}')) = \frac{dS'}{x_\partial^2} [\mathbf{n}' \cdot \frac{\mathbf{x}_\partial}{x_\partial}]. \quad (35)$$

Taking the integral in formula (34) in terms of the solid angle (35) gives

$$p_+^D(\mathbf{x}, t) \approx -a_p \int_0^{T_s} dt' \int_{\partial\nu} d\Omega_{\mathbf{x}}(S'(\mathbf{x}')) x_\partial^2 g_+^D(\mathbf{x}_\partial, t_\partial) \left[\frac{1}{c} \frac{\partial}{\partial t'} p(\mathbf{x}', t') \right], \quad g_+^D(\mathbf{x}_\partial, t_\partial)|_{\partial\nu} = 0. \quad (36)$$

As discussed above, the *solid angle* included in the formula (36), or it equivalent *obliquity factor* $\mathbf{n}' \cdot (\mathbf{x}_\partial/x_\partial)$, can be approximated using ray-based methods very straightforwardly, but approximating this factor is not straightforward using a full-wave approach. It must be reminded that $a_p = 1$ and $a_p = 2$ are used for *Kirchhoff-Helmholtz* and *Rayleigh-Sommerfeld* formulae, respectively.

5. NUMERICAL APPROXIMATION TO THE WAVE EQUATION IN THE TIME DOMAIN

This section describes numerical approaches for approximation of the wave equation (1). First, this section explains a semi-numerical approximation to the time-domain *Primary solution* (12) to the wave equation, i.e., a solution to the wave equation (2) which links a causal wavefield directly to the radiation source s . Then, it will be described how the derived system for semi-numerical approximation to the primary solution to the wave equation can be generalised to solve the wave equation in terms of a surface source, specifically the integral formulae (32) and (34). It will be shown that the key step is how to define the mass source and include it in the derived semi-numerical systems for solving the wave equation. Then, the procedure for full-discretisation of the derived numerical systems for solving the wave equation will be explained.

5.1. Systems of wave equations for solving the time-domain Primary solution. This section describes the systems for a semi-numerical approximation to the wave equation, specifically it describes how to approximate the time-domain *Primary solution* derived in Eq. (12). To do this, the term including the spatial gradients is transferred to the right-hand-side of the wave equation (1) to obtain

$$\frac{1}{c^2} \frac{\partial^2}{\partial t^2} p(\mathbf{x}, t) = \rho_0 \nabla \cdot \left[\frac{1}{\rho_0} \nabla p(\mathbf{x}, t) \right] + s(\mathbf{x}, t), \quad (37)$$

where we remind that s is assumed to have finite volume and radiate within a finite time, and it is square-integrable in a space-time domain.

5.1.1. System of second-order wave equations. Solving the second-order wave equation (37) directly gives the system of wave equations

$$\begin{aligned} \frac{\partial}{\partial t} \rho'(\mathbf{x}, t) &= \rho_0 \nabla \cdot \left[\frac{1}{\rho_0} \nabla p(\mathbf{x}, t) \right] + s(\mathbf{x}, t) \\ \frac{\partial}{\partial t} \rho(\mathbf{x}, t) &= \rho'(\mathbf{x}, t) \\ p(\mathbf{x}, t) &= c(\mathbf{x})^2 \rho(\mathbf{x}, t), \end{aligned} \quad (38)$$

where the first and second lines are approximated via numerical integration in time. Note that by assuming a homogeneous ρ_0 , the first term in the right-hand-side of Eq. (37) is reduced to $\nabla^2 p = \nabla \cdot \nabla p$. The physical quantity given as an input to the wave equation is the *mass source* s_m , which relates to the radiation source s in the form

$$s(\mathbf{x}, t) = \frac{\partial}{\partial t} s_m(\mathbf{x}, t) \Leftrightarrow s_m(\mathbf{x}, t) = \int_0^t dt' s(\mathbf{x}, t'). \quad (39)$$

The mass source s_m has units $\text{kg m}^{-\text{d}}\text{s}^{-1}$. Accordingly, the semi-numerical representation of the second-order wave equation (37) in terms of the mass source gives

$$\begin{aligned} \frac{\partial}{\partial t} \rho'(\mathbf{x}, t) &= \rho_0 \nabla \cdot \left[\frac{1}{\rho_0} \nabla p(\mathbf{x}, t) \right] \\ \frac{\partial}{\partial t} \rho(\mathbf{x}, t) &= \rho'(\mathbf{x}, t) + s_m(\mathbf{x}, t) \\ p(\mathbf{x}, t) &= c(\mathbf{x})^2 \rho(\mathbf{x}, t), \end{aligned} \quad (40)$$

5.1.2. System of three-coupled first-order wave equations. It is possible to recast the wave equation (37) as coupled first-order wave equations, which yield the time stepping system [2]

$$\begin{aligned} \frac{\partial}{\partial t} \mathbf{u}(\mathbf{x}, t) &= -\frac{1}{\rho_0} \nabla p(\mathbf{x}, t) \\ \frac{\partial}{\partial t} \rho(\mathbf{x}, t) &= -\rho_0 \nabla \cdot \mathbf{u}(\mathbf{x}, t) + [s_m(\mathbf{x}, t) = \int_0^t dt' s(\mathbf{x}, t')] \\ p(\mathbf{x}, t) &= c(\mathbf{x})^2 \rho(\mathbf{x}, t). \end{aligned} \quad (41)$$

With some minor algebra, it can be shown that the solution to the second-order systems (38) and (40), and the coupled first-order system (41), all match. These systems all approximate the time-domain *Primary solution*, and link the pressure field p with units $\text{kg m}^{2-\text{d}}\text{s}^{-2}$ (or Pascal) directly to a radiation source s with units $\text{kg m}^{-\text{d}}\text{s}^{-2}$ (or Pascal times m^{-2}), or to a mass source $(\partial/\partial t)s_m$ with units $\text{kg m}^{-\text{d}}\text{s}^{-1}$ (or Pascal times m^{-2}s). When these numerical systems are used for solving the primary formula (12), the source is defined over a finite and d -dimensional space. It is reminded

that the *Primary solution* to the wave equation represents the wavefield as a superposition of actions of Green's function over the volume and radiation time of the source.

5.2. A generalisation to the mass source. The semi-numerical systems introduced in section 5.1 was used for solving the primary formula (12) in terms of a d -dimensional radiation source s . However, in the time-domain monopole integral formula (32), the source is defined in terms of a surface function, which can be a singlet source in terms of $-(\partial/\partial\mathbf{n})p = \rho_0\partial u^{\mathbf{n}}/\partial t$ with $u^{\mathbf{n}} = \mathbf{u} \cdot \mathbf{n}$ and \mathbf{n} an outward unit vector normal to the surface. In addition, for the time-domain dipole integral formula (34), the surface source is defined as a doublet source in terms of pressure p , which was then replaced by a singlet source $1/c (\partial/\partial t)p$. Here, the semi-numerical systems introduced in section 5.1 are extended to solve these analytic formulae. To achieve this goal, a generalised mass source, which is defined based on the analytic formula we approximate, is defined. To do that, we start with dividing the space of support of the source, which can be either a d -dimensional space ν_s or a $d - 1$ -dimensional space $\partial\nu$ (for $d = 3$, a bounding surface or a flat plane), into a union of non-overlapping primitive shapes (elements) e , $e \in \{1, \dots, N_e\}$ with vertices j , $j \in \{1, \dots, N_j\}$.¹ Accordingly, $l(e)$ denotes the set of vertices connected to element e , and has $N_{l(e)}$ members. For $d = 3$ and a volumetric (resp. surface) source, the elements are set tetrahedrons (resp. triangles). The volumetric (resp. surface) source for $d = 3$ is reduced to surface (resp. line) source for $d = 2$.

5.2.1. \mathcal{S}_m in terms of a d -dimensional radiation source s . For numerically approximating the time-domain primary formula (12), a generalised mass source in terms of the radiation source s is defined in the form

$$\begin{aligned} \mathcal{S}_{(m,s)}(\mathbf{x}, t) &= \int_{\nu_s} d\mathbf{x}' \delta(\mathbf{x} - \mathbf{x}') \left[\int_0^t dt' q_s(\mathbf{x}', t') \right] \\ &\approx \frac{1}{N_{l(e)}} \sum_{e=1}^{N_e} v_e \sum_{j \in l(e)} \delta(\mathbf{x} - \mathbf{x}_j) \left[\int_0^t dt' q_s(\mathbf{x}_j, t') \right], \quad \mathbf{x}_j \in \nu_s, \end{aligned} \quad (42)$$

where

$$q_s(\mathbf{x}, t) = s(\mathbf{x}, t). \quad (43)$$

In Eq. (42), for $d = 3$ (resp. $d = 2$), the element e is a tetrahedron (resp. triangle) with v_e the volume (resp. area) of element e , and $N_{l(e)} = d + 1$, i.e., e has $d + 1$ connected vertices. Let us recheck the units. $\int_0^t dt' s(\mathbf{x}, t')$ has units $\text{kgm}^{-d}\text{s}^{-1}$. In addition, $\delta(\mathbf{x} - \mathbf{x}')$ and the elemental volume (resp. area) $d\mathbf{x}'$ have units m^{-d} and m^d , respectively. Their product gives a mass source with units $\text{kgm}^{-d}\text{s}^{-1}$.

5.2.2. \mathcal{S}_m in terms of a $d - 1$ -dimensional singlet source $\partial p/\partial\mathbf{n}$. For numerically approximating the monopole integral formula (32), a generalised mass source in terms of the normal derivative of

¹Here, it will be assumed that the source is piecewise homogeneous over each finite element. For integration over the space of the source, more accurate numerical integration schemes are available in the literature and can be used by readers, for example an assumption of piecewise linearity is more accurate than piecewise homogeneity. However, the focus of this manuscript is not on numerical approaches for integration over a volumetric or surface source. Note that in practical settings, the source is quantified through experiments and the analytic function of source is rarely available.

pressure over the $d - 1$ -dimensional space $\partial\nu$ is defined in the form

$$\begin{aligned} \mathcal{S}_{(m,\partial p/\partial \mathbf{n})}(\mathbf{x}, t) &= a_p \int_{\partial\nu} dS'(\mathbf{x}') \delta(\mathbf{x} - \mathbf{x}') \left[\int_0^t dt' q_{\partial p/\partial \mathbf{n}}(\mathbf{x}', t') \right] \\ &\approx \frac{a_p}{N_{l(e)}} \sum_{e=1}^{N_e} s_e \sum_{j \in l(e)} \delta(\mathbf{x} - \mathbf{x}_j) \left[\int_0^t dt' q_{\partial p/\partial \mathbf{n}}(\mathbf{x}_j, t') \right], \quad \mathbf{x}_j \in \partial\nu, \end{aligned} \quad (44)$$

where

$$q_{\partial p/\partial \mathbf{n}}(\mathbf{x}, t) = -\frac{\partial}{\partial \mathbf{n}} p(\mathbf{x}, t). \quad (45)$$

In Eq. (44), for $d = 3$ (resp. $d = 2$), the element e is a triangle (resp. a line) with s_e the area (resp. length) of element e , and $N_{l(e)} = d$, i.e., e has d connected vertices. It is reminded that for the *Kirchhoff-Helmholtz* formula and for $d = 3$ (resp. $d = 2$), $\partial\nu$ is a closed surface (resp. line) bounding the volume (resp. area) ν_s , the support of the radiation source s , and $a_p = 1$ is set. (cf. section 2.2.2.) Furthermore, for approximating the *Rayleigh-Sommerfeld* formula, $\partial\nu$ has been assumed a bounding plane, and $a_p = 2$ is set. (cf. section 3.2.3.) Let us recheck the units now. $\int_0^t dt' (\partial/\partial \mathbf{n})p(t')$ has units $\text{kgm}^{1-d}\text{s}^{-1}$. In addition, $\delta(\mathbf{x} - \mathbf{x}')$ has units m^{-d} , and the elemental area (resp. length) dS' has units m^{d-1} . Their product provides a mass source with units $\text{kgm}^{-d}\text{s}^{-1}$.

5.2.3. \mathcal{S}_m in terms of a $d - 1$ -dimensional singlet source $\rho_0 \mathbf{u}^{\mathbf{n}}$. It may be more convenient to define the monopole formula (32) in terms of the normal velocity via a replacement $(\partial/\partial \mathbf{n})p = -\rho_0(\partial/\partial t)u^{\mathbf{n}}$, where $u^{\mathbf{n}} = u \cdot \mathbf{n}$ with \mathbf{n} a unit vector outwardly normal to the surface. Accordingly, our generalised mass source in terms of $u^{\mathbf{n}}$ is defined as

$$\begin{aligned} \mathcal{S}_{(m,u^{\mathbf{n}})}(\mathbf{x}, t) &= a_p \int_{\partial\nu} dS'(\mathbf{x}') \delta(\mathbf{x} - \mathbf{x}') q_{u^{\mathbf{n}}}(\mathbf{x}', t) \\ &\approx \frac{a_p}{N_{l(e)}} \sum_{e=1}^{N_e} s_e \sum_{j \in l(e)} \delta(\mathbf{x} - \mathbf{x}_j) q_{u^{\mathbf{n}}}(\mathbf{x}_j, t), \quad \mathbf{x}_j \in \partial\nu, \end{aligned} \quad (46)$$

where

$$q_{u^{\mathbf{n}}}(\mathbf{x}, t) = \rho_0 u^{\mathbf{n}}(\mathbf{x}, t). \quad (47)$$

Considering that $\rho_0 u^{\mathbf{n}}$ has the units $\text{kgm}^{1-d}\text{s}^{-1}$, the same as $\int_0^t dt' (\partial/\partial \mathbf{n})p(t')$ in Eq. (44), both sides of equation (46) have units $\text{kgm}^{-d}\text{s}^{-1}$.

5.2.4. \mathcal{S}_m in terms of a $d - 1$ -dimensional doublet source p . By an assumption $\mathbf{n}' \cdot (\mathbf{x}_{\mathfrak{d}}/x_{\mathfrak{d}}) = 1$, i.e., ignoring the *obliquity factor*, which may not be true, a generalised mass source is defined in the form

$$\begin{aligned} \mathcal{S}_{(m,p)}(\mathbf{x}, t) &= a_p \int_{\partial\nu} dS'(\mathbf{x}') \delta(\mathbf{x} - \mathbf{x}') q_p(\mathbf{x}', t) \\ &\approx \frac{a_p}{N_{l(e)}} \sum_{e=1}^{N_e} s_e \sum_{j \in l(e)} \delta(\mathbf{x} - \mathbf{x}_j) q_p(\mathbf{x}_j, t), \quad \mathbf{x}_j \in \partial\nu, \end{aligned} \quad (48)$$

where

$$q_p(\mathbf{x}, t) = -\frac{1}{c} p(\mathbf{x}, t). \quad (49)$$

Note that p is a doublet surface source, but q_p is a singlet surface source. In equation (48), $(1/c) p(\mathbf{x}, t)$ has units $\text{kgm}^{1-d}\text{s}^{-1}$, $\delta(\mathbf{x} - \mathbf{x}')$ has units m^{-d} , and the elemental area (or length for $d = 2$) dS' has units m^{d-1} . Their product gives a mass source in units $\text{kgm}^{-d}\text{s}^{-1}$. It must be emphasized again that the assumption $\mathbf{n}' \cdot (\mathbf{x}_\partial / x_\partial) = 1$ does not hold, and an efficient approximation of this parameter is a limitation for full-wave methods compared to analytic or ray-based methods. The same approach is used for defining the mass source associated with a numerical approximation of a dipole version of *back-projection* formula (15), which is defined in terms of a Green's function satisfying a homogeneous *Dirichlet* condition over a measurement surface $\partial\nu$.

5.3. Full-discretisation on a regular grid. This section explains the procedure for discretisation of systems of wave equations derived in section 5.1 with an emphasis on inclusion of source in the wave equation. Here, compared to section 5.1, the mass source s_m in terms of a d -dimensional source s will be replaced with a generalised mass source \mathcal{S}_m , which was defined in section 5.2. For approximating the time-domain primary formula (12), this generalised mass source is defined in terms of s , which has a d -dimensional support in space. For approximating the time-domain *monopole* formula (32), the generalised mass source \mathcal{S}_m is defined in the form of a singlet source in terms of $-(\partial/\partial\mathbf{n})p$ or it equivalent $\rho_0\partial u^\mathbf{n}/\partial t$. For approximating the time-domain *dipole* formula (34), the generalised mass source \mathcal{S}_m is defined in the form $(1/c)(\partial p/\partial t)$ over a $d - 1$ -dimensional surface. The full-discretisation will be described for the system of three-coupled first-order wave equations (41), and an extension to the second-order wave equation systems (38) and (40) will be straightforward.

5.3.1. Discretised algorithm. Let $\mathbf{X} = \{X^\zeta : \zeta \in \{1, \dots, d\}\}$ with ζ the Cartesian coordinates and Δx^ζ the grid spacing along the Cartesian coordinate ζ . Also, $\mathbf{t} \in \{1, \dots, N_t\}$ stands for the times sampled within the measurement time $t \in \{0, \dots, T\}$ with N_s the sampled time associated with the turn-off time of radiation of source, T_s . Here, a bar notation will be used for specifying the quantities in the full-discretised domain. Accordingly, a discretisation of the system of wave equations (41) on a grid staggered in space and time is outlined in algorithm 1. In algorithm 1, $\Lambda^\zeta = e^{-\alpha^\zeta \Delta t/2}$

Algorithm 1 Full-discretisation at time step $\mathbf{t} \in \{1, \dots, N_t - 1\}$

- 1: **Input:** $\bar{c}, \bar{\rho}_0, \Delta t, \Lambda^\zeta$ ($\zeta \in \{1, \dots, d\}$), $\bar{\mathcal{S}}_m^\zeta(\mathbf{X}, \mathbf{t} + \frac{1}{2})$
 - 2: **Initialise:** $p(\mathbf{X}, 1) = 0$, $\bar{\rho}(\mathbf{X}, 1) = 0$, $\bar{\mathbf{u}}(\mathbf{X}, \frac{1}{2}) = 0$, $\forall \mathbf{X}$ ▷ Set Cauchy conditions
 - 3: Start at iteration $\mathbf{t} = 1$ ▷ Iterate
 - 4: Record $\bar{p}(\mathbf{X}, \mathbf{t})$ ▷ Record pressure
 - 5: $\bar{\mathbf{u}}^\zeta(\mathbf{X}, \mathbf{t} + \frac{1}{2}) \leftarrow \Lambda^\zeta \left[\Lambda^\zeta \bar{\mathbf{u}}^\zeta(\mathbf{X}, \mathbf{t} - \frac{1}{2}) - \Delta t \frac{1}{\bar{\rho}_0(\mathbf{X})} \frac{\partial}{\partial \zeta} \bar{p}(\mathbf{X}, \mathbf{t}) \right]$ ▷ Update \mathbf{u}
 - 6: $\bar{\rho}(\mathbf{X}, \mathbf{t} + 1) \leftarrow \Lambda^\zeta \left[\Lambda^\zeta \bar{\rho}(\mathbf{X}, \mathbf{t}) - \Delta t \bar{\rho}_0(\mathbf{X}) \frac{\partial}{\partial \zeta} \bar{\mathbf{u}}_\zeta(\mathbf{X}, \mathbf{t} + \frac{1}{2}) \right] + \Delta t \bar{\mathcal{S}}_m^\zeta(\mathbf{X}, \mathbf{t} + \frac{1}{2})$ ▷ Update ρ
 - 7: $\bar{p}(\mathbf{X}, \mathbf{t} + 1) \leftarrow \bar{c}(\mathbf{X})^2 \sum_{\zeta=1}^d \bar{\rho}^\zeta(\mathbf{X}, \mathbf{t} + 1)$ ▷ Update p
 - 8: Terminate at iteration $\mathbf{t} = N_t - 1$
 - 9: Record $\bar{p}(\mathbf{X}, N_t)$ ▷ Record pressure at $t = T$
 - 10: **Output:** $\bar{p}(\mathbf{X}, \mathbf{t})$ ($\mathbf{t} \in \{1, \dots, N_t\}$) ▷ Recorded pressure at $t \in [0, T]$.
-

is a direction-dependent Perfectly-matched layer (PML) with α^ζ the absorption coefficient of the PML along the Cartesian coordinate ζ . In addition, $\bar{\mathcal{S}}_m^\zeta = (1/d)\bar{\mathcal{S}}_m$, where $\bar{\mathcal{S}}_m$ is computed via a discretisation of formulae (42), (44), (46) or (48).

5.3.2. *Interpolation operator.* For defining the discretised version of the mass source, a dimensionless map $b(\mathbf{X}, \mathbf{x})$, which interpolates a function from any arbitrary points \mathbf{x} onto any grid points \mathbf{X} , will be used. This interpolation map can be defined in different ways. One choice is based on a *Fourier* interpolation. Using a Fourier interpolation approach for a discretised grid with N_n^ζ grid points along the Cartesian coordinate ζ and with N_n^ζ an odd scalar, the interpolation from any arbitrary points \mathbf{x} which lie in the grid onto any grid points \mathbf{X} can be done using the formula

$$b^{\text{fourier}}(\mathbf{X}, \mathbf{x}) \approx \prod_{\zeta=1}^d \frac{\sin\left(\frac{\pi(X^\zeta - x^\zeta)}{\Delta x^\zeta}\right)}{N_n^\zeta \sin\left(\frac{\pi(X^\zeta - x^\zeta)}{N_n^\zeta \Delta x^\zeta}\right)}, \quad (50)$$

where $\prod_{\zeta=1}^d$ denotes the product of functions associated with the Cartesian coordinates [73]. Computing the interpolation formula (50) is computationally very expensive, because it requires storing an associated full matrix. For sufficiently large N^ζ , sparse interpolation maps can be obtained using an approximated interpolation map

$$b^{\text{fourier}}(\mathbf{X}, \mathbf{x}) \approx \prod_{\zeta=1}^d \text{sinc}\left(\frac{\pi(X^\zeta - x^\zeta)}{\Delta x^\zeta}\right), \quad (51)$$

for which magnitudes smaller than a threshold are neglected [73]. A very sparse map can be obtained using a *trilinear* approach, but this map is less accurate than the *Fourier* approach.

5.3.3. *Discretised mass source.* Using this interpolation map, the discretisation of formula (42) gives

$$\bar{\mathcal{S}}_{(m,s)}(\mathbf{X}, \mathbf{t}) \approx \frac{a_p \Delta t}{N_{l(e)} \Delta x^1 \dots \Delta x^d} \sum_{e=1}^{N_e} v_e \sum_{j \in l(e)} b(\mathbf{X}, \mathbf{x}_j) \sum_{t'=1}^t \bar{s}(\mathbf{x}_j, t'), \quad (52)$$

where $a_p = 1$. The discretisation of formula (44) gives

$$\bar{\mathcal{S}}_{(m,\partial p/\partial \mathbf{n})}(\mathbf{X}, \mathbf{t}) \approx \frac{a_p \Delta t}{N_{l(e)} \Delta x^1 \dots \Delta x^d} \sum_{e=1}^{N_e} s_e \sum_{j \in l(e)} b(\mathbf{X}, \mathbf{x}_j) \sum_{t'=1}^t \left[-\frac{\partial}{\partial \mathbf{n}} \bar{p}(\mathbf{x}_j, t') \right], \quad (53)$$

where $a_p = 1$ and $a_p = 2$ for the *Kirchhoff-Helmholtz* and *Rayleigh-Sommerfeld* formulae, respectively. The discretisation of formula (46) gives

$$\bar{\mathcal{S}}_{(m,u^n)}(\mathbf{X}, \mathbf{t}) \approx \frac{a_p \bar{\rho}_0}{N_{l(e)} \Delta x^1 \dots \Delta x^d} \sum_{e=1}^{N_e} s_e \sum_{j \in l(e)} b(\mathbf{X}, \mathbf{x}_j) \bar{u}^n(\mathbf{x}_j, \mathbf{t}), \quad (54)$$

where it has been assumed that the support of the surface source resides in a medium with homogeneous ambient density ρ_0 , and a_p is set the same as in Eq. (53). The discretisation of formula (48) gives

$$\bar{\mathcal{S}}_{(m,p)}(\mathbf{X}, \mathbf{t}) \approx \frac{a_p}{N_{l(e)} \bar{c} \Delta x^1 \dots \Delta x^d} \sum_{e=1}^{N_e} s_e \sum_{j \in l(e)} b(\mathbf{X}, \mathbf{x}_j) \left[-\bar{p}(\mathbf{x}_j, \mathbf{t}) \right], \quad (55)$$

where it is assumed that the support of the surface source resides in a medium with homogeneous sound velocity c , and a_p is set the same as in Eq. (53). Note that in these discretised formulae, we have used

$$\bar{\delta}(\mathbf{X} - \mathbf{x}_0) q(\mathbf{x}_0) \approx \frac{1}{\Delta x^1 \dots \Delta x^d} b(\mathbf{X}, \mathbf{x}_0) q(\mathbf{x}_0), \quad (56)$$

which is the function $\delta(\mathbf{x} - \mathbf{x}_0)q(\mathbf{x}_0)$ interpolated onto the discretised grid. Note that all these formulae, equations (52), (53), (54), and (55), transform the integral formulae $\int dt' \int d\mathbf{x}' gq$ or $\int dt' \int dS' gq$ from an arbitrary-shaped or planar surface to a regular computational grid, where q is a volumetric or surface source, respectively. In these formulae, the factors $v_e/(\Delta x^1 \dots \Delta x^d)$ and $s_e/(\Delta x^1 \dots \Delta x^d)$ account for a change of variable of the integral in space from the volume and surface of an element e to a voxel on the regular grid, respectively.

5.3.4. Discretisation of the directional gradients. In this study, a k-space pseudo-spectral approach is used for discretisation of directional gradients of fields included in algorithm 1 [2]. This approach has been used in the open-source *k-Wave* toolbox [3]. However, the steps for including source in the wave equation were modified to match the associated analytical formulae, as discussed above. Note that the explained numerical approaches including algorithm 1 and the numerical results which will be presented in the next section, are independent of the approach taken for discretising directional gradients of fields.

6. NUMERICAL RESULTS

This section compares an analytic solution to the wave equation to its full discretisation using algorithm 1. For the sake of generality, this comparison is done for a single point, i.e., one vertex $j = j_0$ with position \mathbf{x}_{j_0} . By assuming the source q on a position \mathbf{x}_{j_0} , the time-domain analytic formulae (32) and (34) are reduced to an analytic action

$$a_p \int dt' g_+(\mathbf{x} - \mathbf{x}_{j_0}, t - t') q^{\text{point}}(\mathbf{x}_{j_0}, t'). \quad (57)$$

As discussed in section 3, the frequency-domain version of the action (57) at frequency ω gives

$$a_p G_+(\mathbf{x} - \mathbf{x}_{j_0}, \omega) Q^{\text{point}}(\mathbf{x}_{j_0}, \omega), \quad (58)$$

where it is reminded that G_+ is the frequency-domain *outgoing* (causal) Green's function, and is analytically calculated using the formulae (19) or (21) in a 3D or 2D medium, respectively. A full-discretised approximation of this action can be done using algorithm 1. For a source on a single point, the formulae (42) and (44) are reduced to

$$\mathcal{S}_{(m, \{s, \partial p / \partial \mathbf{n}\})}^{\text{point}}(\mathbf{x}, t) = a_p \delta(\mathbf{x} - \mathbf{x}_{j_0}) \left[\int_0^t dt' q_{\{s, \partial p / \partial \mathbf{n}\}}^{\text{point}}(\mathbf{x}_{j_0}, t') \right], \quad (59)$$

and the formulae (46) and (48) are reduced to

$$\mathcal{S}_{(m, \{u^n, p\})}^{\text{point}}(\mathbf{x}, t) = a_p \delta(\mathbf{x} - \mathbf{x}_{j_0}) q_{\{u^n, p\}}^{\text{point}}(\mathbf{x}_{j_0}, t). \quad (60)$$

Here, the superscript “point” has been used to indicate that the mass source is not a physical quantity for a source defined on a single point, but this simple representation is sufficient for comparing the action of analytic Green's function with its full-discretisation using algorithm 1.²

²As discussed at the beginning of section 2, the solution of the wave equation (1) is based on an assumption that the source is square-integrable in space and time. However, this condition is not satisfied for a point source. Accordingly, for a point source, all quantities included in the semi-numerical systems introduced in section 5.1 including the solution are not physical quantities. For this simplified and nonphysical numerical experiment using a d -dimensional radiation source s (resp. a $d - 1$ -dimensional surface source) on a single point, these quantities will have units m^{-d} (resp. m^{1-d}) times the units of physical quantities associated with a physical source and with finite volume (or area), as discussed in section 5.2. Accordingly, assuming transducers, for example Fabry-Perot sensors, as points, for example in the *back-projection* operator in photo-acoustic tomography, may not make sense. Note that a grid point does not represent a point in a continuous (or real) space, and represents a volume equal to the volume of a voxel and with centre on that grid point. Therefore, for including source in the semi-numerical system associated with a

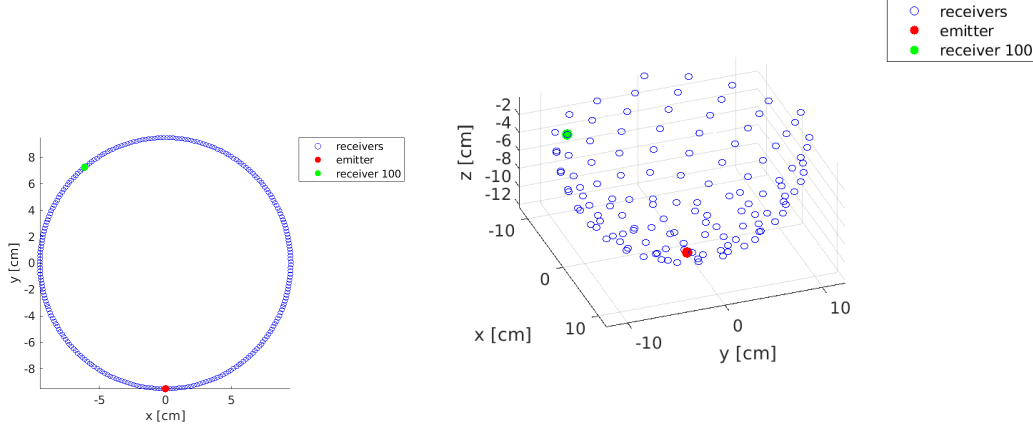


FIGURE 1. Transducers: (a) 2D medium, (b) 3D medium.

A full discretisation of formula (59) gives

$$\bar{S}_{(m,\{s,\partial p/\partial \mathbf{n}\})}^{\text{point}}(\mathbf{X}, \mathbf{t}) \approx \frac{a_p \Delta t}{\Delta x^1 \dots \Delta x^d} b(\mathbf{X}, \mathbf{x}_{j_0}) \sum_{t'=1}^t \bar{q}_{\{s,\partial p/\partial \mathbf{n}\}}^{\text{point}}(\mathbf{x}_{j_0}, \mathbf{t}'). \quad (61)$$

Now, the analytic action (57) for a point source q^{point} on position \mathbf{x}_{j_0} will be compared to its numerical approximation using algorithm 1, in which the discretised mass source has been approximated using Eq. (61). Because the source is assumed point, the spatial integral has been dropped, and therefore, the source q^{point} can be assumed either a radiation point source s with a d -dimensional support, or normal pressure derivative $-(\partial/\partial \mathbf{n})p$ on a single point over a $d-1$ -dimensional space (surface for $d=3$). By ignoring the factor a_p in Eq. (61), both types of sources will give the same output p^{point} , which will be a nonphysical quantity with units m^{-d} Pascal for a source s or with units m^{1-d} Pascal for a source $-(\partial/\partial \mathbf{n})p$. (By ignoring the time integral in (61), the source q can be assumed a surface source $\rho_0 u^{\mathbf{n}}$ or $-(1/c)p$ on a single point on a surface, but what will be approximated below is formula (61), which includes the time integral, and uses $a_p = 1$ for generality.) As discussed in section 5.3.4, the gradient of the fields are approximated using a k-space pseudo-spectral approach [2]. To do this, an open-source toolbox, k-Wave [3], was used, but the step for including the source in the wave equation was modified so that it approximates the analytic action (57).

6.1. Wave simulation for a 2D medium. Wave simulations were performed on a grid with the same grid spacing 0.4 mm along all Cartesian coordinates. The grid spacing is arbitrary, but it must be chosen sufficiently small that the frequency spectrum of the source is supported by the grid. One emitter and 256 receivers, which were assumed single points, were placed on a ring with a radius of 9.5 cm. The interpolations between position of the emitter/receivers and grid points were performed using the approximated formula (51). The sound speed was set homogeneous and 1500 ms^{-1} . The emitter was placed on the position $\mathbf{x}_{j_0} = [0, -9.5] \text{ cm}$. Figure 1(a) shows the emitter and receivers by the red and blue colours, respectively.

back-projection operator, the pressure p measured on a transducer cannot be defined on a single grid point, because a grid point represents a volume, but pressure is a doublet source, and must be defined over a surface, not volume.

The simulations were performed using three different source pulses $q_{\{s, \partial p / \partial \mathbf{n}\}}^{\text{point}}$ within a time $[0, T]$ with $T = 163.26 \mu\text{s}$. Here, $q_{\{s, \partial p / \partial \mathbf{n}\}}^{\text{point}}$ denotes a nonphysical source, which can be either s or $-(\partial / \partial \mathbf{n})p$ on a single point. Figures 2(a), 2(b) and 2(c) show the source pulses 1, 2 and 3, respectively. A low-pass filter was applied on each source pulse using the *filterTimeSeries.m* function in the k-Wave to ensure that the frequency spectrum of the pulse be smaller than the maximum frequency supported by the computational grid and the maximum absolute amplitudes of the pulses were then normalised. The source pulses have been shown after low-pass filtering and normalisation in amplitude. The maximum frequency supported by the grid for the wave simulation can be determined by the *Shannon-Nyquist* limit [2]. For a homogeneous medium with sound speed c , the maximum supported frequency is determined by [5]

$$f_{\max} = \frac{c}{2\Delta x}. \quad (62)$$

Here, considering that $\Delta x = 0.4 \text{ mm}$ and $c = 1500 \text{ ms}^{-1}$ and homogeneous, the computed f_{\max} was 1.875 MHz. The simulations were done using different Courant–Friedrichs–Lewy (CFL) numbers. The simulation for source pulse 1 was performed using a CFL number 0.1, which gives a time spacing $\Delta t = 25.25 \text{ ns}$, equivalent to a sampling rate of 39.6 MHz. The simulation for source pulse 2 was performed using a CFL number 0.2, which gives a time spacing 50.51 ns, equivalent to a sampling rate of 19.80 MHz. The simulation 3 was performed using a CFL number 0.3, which is equivalent to a time spacing 75.76 ns and a sampling rate of 13.20 MHz. Figures 2(d), 2(e) and 2(f) show the amplitude and phase of the source pulses in the frequency domain for the simulations 1, 2 and 3, respectively. For each simulation, the simulated field was recorded at the sampled times and on the receivers, and the recorded signals in time on the receivers were then decomposed into the frequency components (phase and amplitude) using a Fourier Transform operator. As a benchmark, this nonphysical solution field was also analytically calculated using the frequency-domain formula (58), in which the Green’s function was calculated using Eq. (21).

Figures 3(a), 3(b) and 3(c) show the amplitude of the solution field produced after radiation of the emitter (the red circle in figure 1(a)) and recorded on the receiver 100 (the green circle in figure 1(a)) as a function of temporal frequency, when the source pulses 1, 2 and 3 were used, respectively. As shown in these figures, the frequency-domain amplitudes of the solution field approximated using algorithm 1 and a mass source computed using Eq. (61) (the modified k-Wave) match the amplitudes analytically calculated using the Green’s formula (58) for all frequencies. The amplitudes approximated by giving the same input to the original k-Wave were added to the plot in order to show how modifying the toolbox computes a mass source matching the discretised formula (61), which is a discretisation of Eq. (59), and gives the analytical action (57) in the time-domain as the output. It must be reminded that the details about the full-discretisation of the wave equation in the original k-Wave is given in the k-Wave manual [5], section 2.4, or [51], Algorithm 1. Specifically, the step taken for including the mass source has been described in the k-Wave manual [5], section 2.4, equations (2.18) and (2.19), or [51], Algorithm 1, line 5.

In the same way, figures 3(d), 3(e) and 3(f) show phases of the solution field recorded on the receiver 100, when the source pulses 1, 2 and 3 were used, respectively. The phases were wrapped to $[-\pi, \pi]$ rad. As shown in these figures, the frequency-domain variants of phases approximated by the modified k-Wave, which approximates Eq. (57) and uses a mass source computed by Eq. (61) which is a discretisation of Eq. (59), and phases analytically calculated using the frequency-domain Green’s formula (58) match for all frequencies.

Figures 4(a), 4(b) and 4(c) show amplitudes of the solution field recorded on all the receivers as a function of distance of receivers to the emitter, when the source pulses 1, 2 and 3 were used,

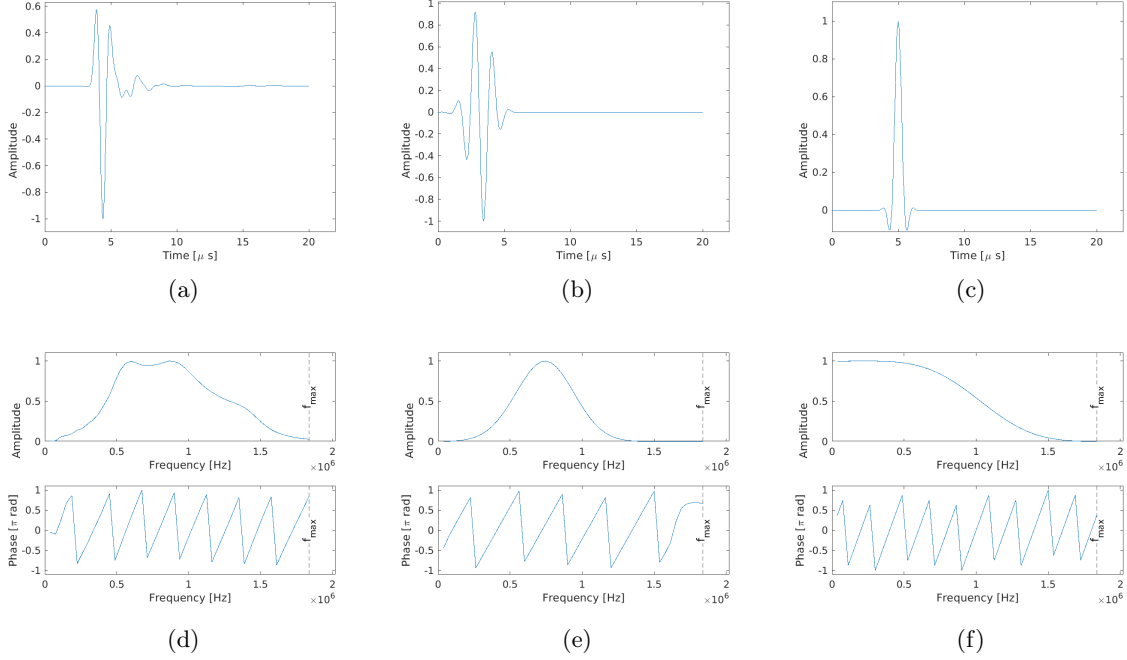


FIGURE 2. 2D medium. The time-domain source pulses on a single point ($q_{\{s,\partial p/\partial \mathbf{n}\}}^{\text{point}}$): a) 1, b) 2 and c) 3. The frequency-domain amplitude and phase of the point sources: d) 1, e) 2 and f) 3.

respectively. In these figures, the amplitudes were computed at the single frequency $f_{\text{max}}/2$ MHz. As shown in these figures, for all these source pulses, the frequency-domain variants of amplitudes computed using the modified k-Wave and using the discretised mass source (61) (red plot), match the analytic solution (58) (green plot). In the same way, figures 4(d), 4(e) and 4(f) show phase of the solution field recorded on all receivers, when the source pulses 1, 2 and 3 were used, respectively. The phases were wrapped to $[-\pi, \pi]$ rad. Note that for the k-Wave simulation, each recorded pressure signal was transformed into the frequency domain. It must be reminded that the plots for which the same inputs are given to the original k-Wave were added only to show the readers how modifying the toolbox and approximating a mass source based on the formula (59), gives an approximation to the analytic action (57) for the associated single-point source.

6.2. Wave simulation for a 3D medium. The wave simulations were performed on a grid with the same grid spacing 0.5 mm along all Cartesian coordinates. The grid spacing must be small sufficiently that the frequency range of the source is supported by the grid. One emitter and 256 receivers, which were assumed points, were placed on a hemisphere with a radius of 12.35 cm, as shown in figure 1(b). The emitter was placed at the bottom of the hemisphere on the position $\mathbf{x}_{j_0} = [1.54, 0, -12.25]$ cm. Figure 1(b) shows the emitter by the red colour and the receivers by the blue colour. The interpolations between the position of the emitter/receivers and the grid points were performed using the formula (51) [3]. The sound speed was set 1500 ms^{-1} and homogeneous. The wave simulations were performed using three different sources $q_{\{s,\partial p/\partial \mathbf{n}\}}^{\text{point}}$ for a time duration $T = 212.2 \mu\text{s}$. Figures 5(a), 5(b) and 5(c) show the source pulses 1, 2 and 3 in time, respectively. Here, a low-pass filter was applied on each source pulse using the *filterTimeSeries.m* function in the

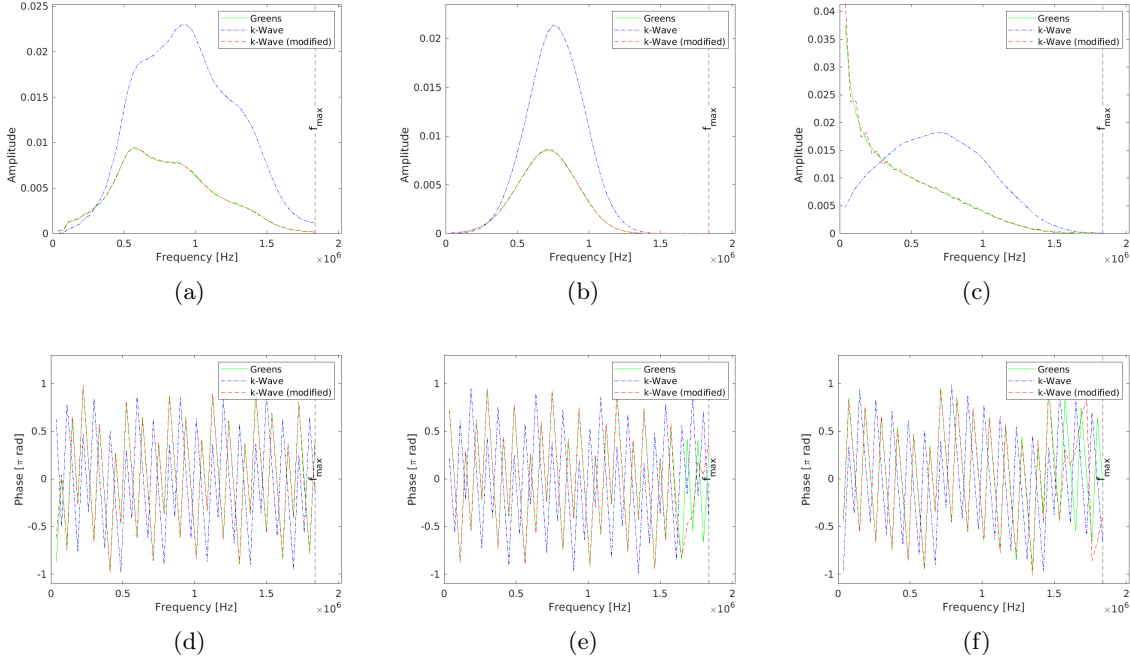


FIGURE 3. 2D medium. The solution field recorded on the point receiver 100 after radiation of the point source (emitter). The solution field was decomposed into amplitude and phase in the frequency domain. Amplitudes for simulation experiments: a) 1, b) 2 and c) 3. Because the source is defined on a single point, the quantities of the wave simulation are not physical and the solution field is not pressure. But an integration over a distribution of point sources using the derived formulae in section 5.2 and their discretisation discussed in section 5.3 will provide a solution field in terms of the pressure and with units of Pascal. Phases for simulation experiments: d) 1, e) 2 and f) 3. The phases were wrapped to $[-\pi, \pi]$ rad. The plots are not for the purpose of a direct comparison with the toolbox, but they show how modifying the toolbox to compute a point mass source (61), which is a discretisation of (59), will approximate the analytic action (57).

k-Wave to ensure that the frequency spectrum of the associated pulse be smaller than the maximum frequency supported by the computational grid, and then the maximum absolute amplitudes of the pulses were normalised. The maximum frequency supported by the grid was $f_{\max} = 1.5$ MHz.

For the simulation using the source pulse 1, the CFL number was set 0.1, which is equivalent to a time spacing $\Delta t = 31.57$ ns and a sampling rate of 31.68 MHz. The simulation 2 was performed using the CFL number 0.2, which gives a time spacing 63.13 ns, equivalent to a sampling rate 15.84 MHz. The simulation using the source pulse 3 was performed using the CFL number 0.3, equivalent to a time spacing 94.70 ns and a sampling rate of 10.56 MHz. Figures 5(d), 5(e) and 5(f) show the amplitudes and phases of the source pulses in the frequency domain for the simulations 1, 2 and 3, respectively. Note that the approach taken for including a discretised version of the mass source in the original k-Wave has been explained in [5], section 2.4., equations (2.18) and (2.19), or [51], Algorithm 1, line 5. The taken approach in the original k-Wave for including the mass source was replaced by the formula (61), which is a discretisation of (59), to represent a nonphysical mass

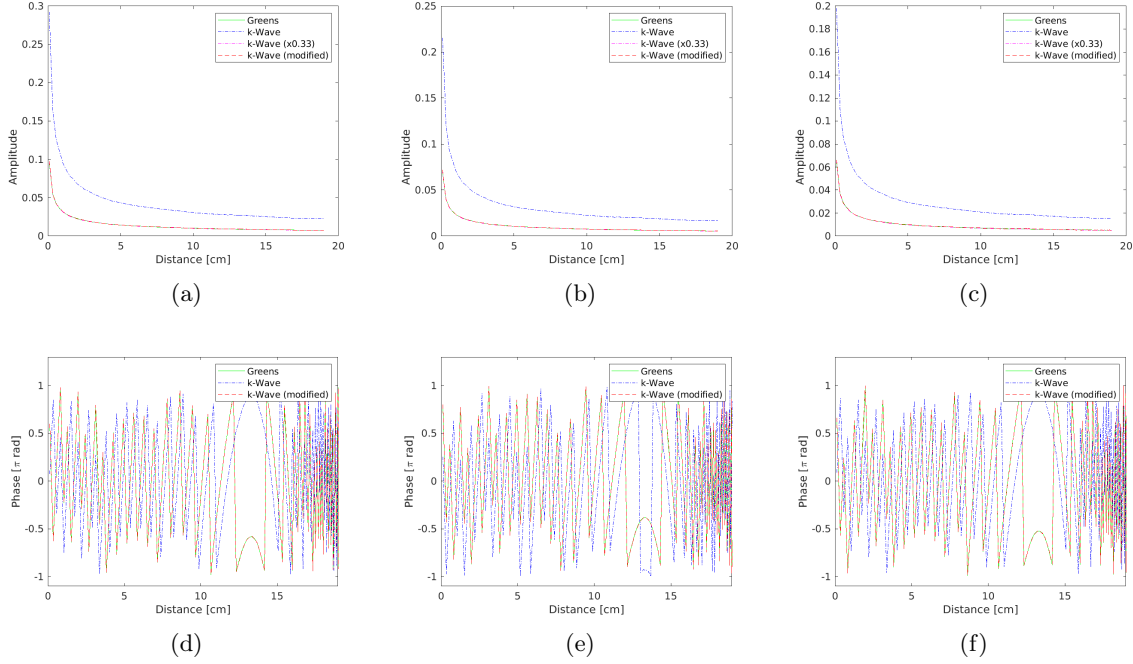


FIGURE 4. 2D medium. The solution field recorded on all the receivers after radiation of the point source (emitter). The solution field was decomposed into amplitude and phase in the frequency domain, and is shown at the single frequency $f_{\max}/2$ as a function of distances of the receivers to the emitter. Amplitudes for simulation experiments: a) 1, b) 2 and c) 3. Phases for simulation experiments: d) 1, e) 2 and f) 3. The phases were wrapped to $[-\pi, \pi]$ rad. The plots are not for the purpose of a direct comparison with the toolbox, but they show how modifying the toolbox to compute a point mass source (61), which is a discretisation of (59), will approximate the analytic action (57).

source on a single point. (An integration using the formulae (52)-(55) over a distribution of point sources will then provide the physical quantities with physical units, as explained in sections 5.2 and 5.3.)

For each simulation, the solution field was recorded on the receivers in time. The recorded time-domain signal on each receiver was then decomposed into the frequency components (phase and amplitude) using a Fourier Transform operator. The solution field was also calculated analytically in the frequency domain using the formula (58), in which the source is transferred to the frequency domain using the same Fourier operator, and the causal (or outgoing) Green's function is calculated using (19). Figures 6(a), 6(b) and 6(c) show the frequency-domain amplitudes of the solution field recorded on receiver 100 (the green circle in figure 1(b)) after excitation of emitter (the red circle in figure 1(b)) using the source pulses 1, 2 and 3, respectively. Because the frequency-domain variant of amplitudes computed by the original k-Wave (blue plot) are much smaller than the amplitudes calculated using Eq. (58) (green plot), a variant of the original k-Wave amplitudes enlarged by a factor 666.7 was also shown by the magenta colour for a better visualisation. It must be reminded that the frequency-domain variants of amplitudes associated with the original k-Wave were added

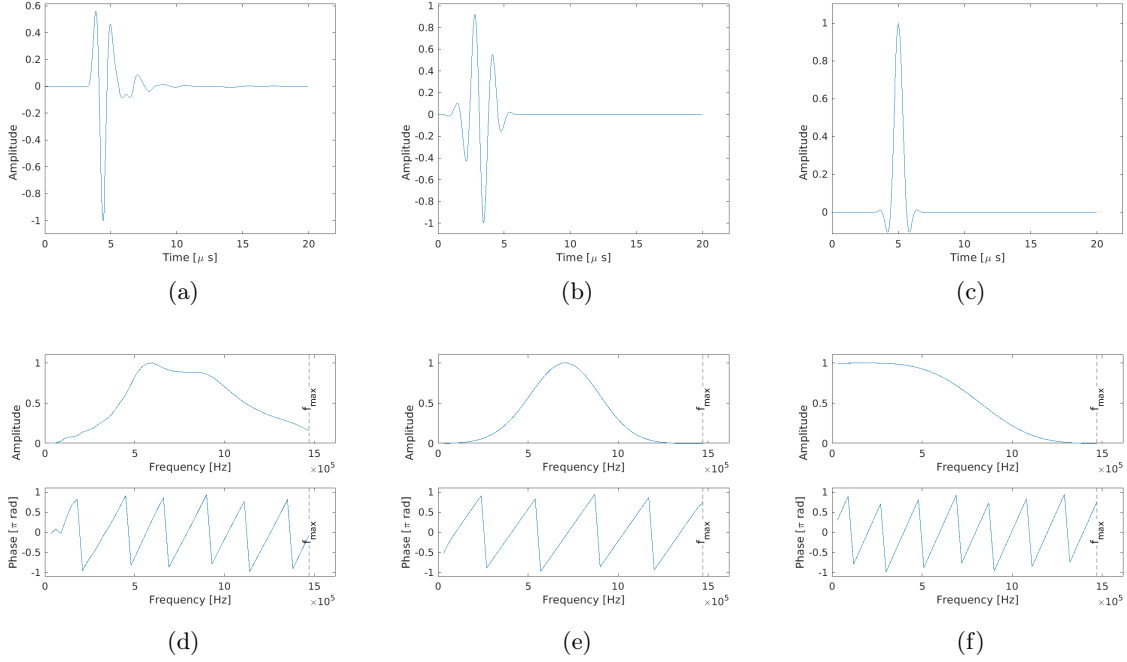


FIGURE 5. 3D medium. The time-domain source pulses on a single point ($q_{\{s,\partial p/\partial \mathbf{n}\}}^{\text{point}}$): a) 1, b) 2 and c) 3. The frequency-domain amplitude and phase of the point sources: d) 1, e) 2 and f) 3.

to show how modifying the mass source using the formula (61) gives the analytic action (57) as an output.

As shown in these figures, the frequency-domain amplitudes approximated using the modified k-Wave match the amplitudes calculated analytically using the frequency-domain Green's formula (58) for all frequencies. In addition, considering Eq. (19), the amplitude of the Green's function in a 3D medium depends only on the distances, and is not changed with frequency. Note that for a nonabsorbing medium, the amplitude of the Green's function represents only geometrical attenuation. (cf. [71] and [72].) Therefore, the fact that the amplitude of the Green's function in (19) is independent of frequency implies that the shape of the ultrasonic pulse on a point should remain unchanged after propagation in the medium. A comparison between the amplitudes of the source pulses in figures 5(d), 5(e) and 5(f) and the approximated amplitudes of the solution field on the receiver 100 in the respective figures 6(a), 6(b) and 6(c) shows that the geometrical attenuation approximated using the modified k-Wave has remained unchanged with frequency. Figures 6(d), 6(e) and 6(f) show the phases of the solution field recorded on the receiver 100, when the source pulses 1, 2 and 3 were used, respectively. The phases were wrapped to $[-\pi, \pi]$ rad. As shown in these figures, the frequency-domain phases approximated using the modified k-Wave and the phases calculated using the frequency-domain Green's formula match for all frequencies.

Figures 7(a), 7(b) and 7(c) show the amplitudes of the solution field recorded on all the receivers as a function of distances of receivers to the emitter, when the source pulses 1, 2 and 3 were used, respectively. In these figures, the amplitudes were computed at the single frequency $f_{\max}/2$ MHz. Because the frequency-domain variants of amplitudes computed by the original k-Wave (blue plot)

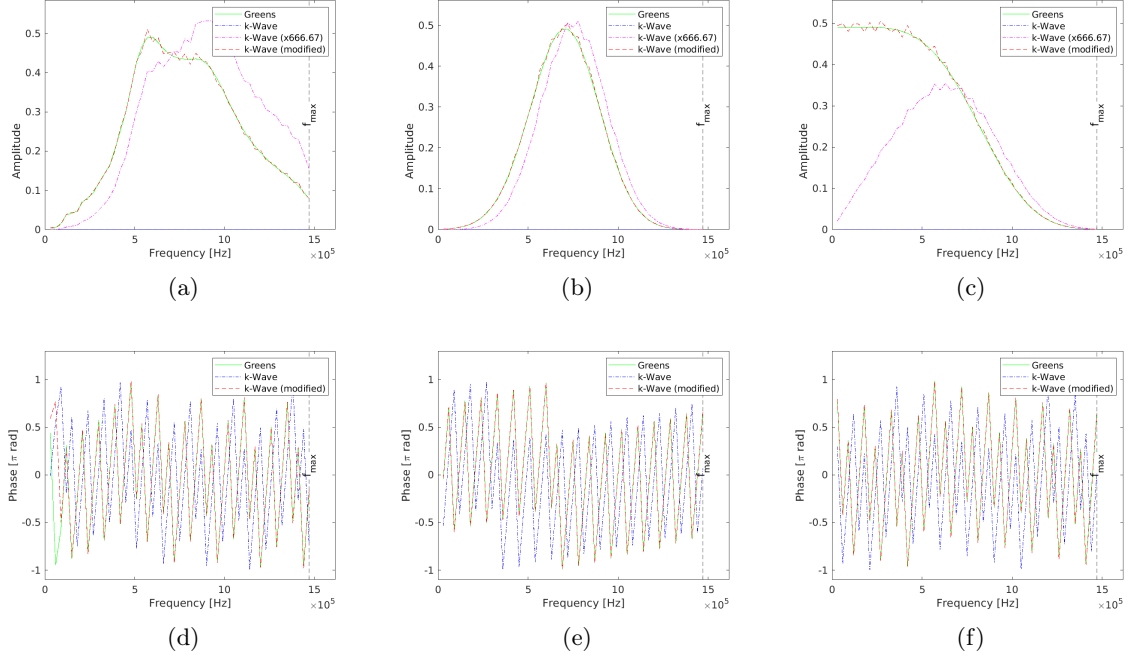


FIGURE 6. 3D medium. The solution field recorded on the point receiver 100 after radiation of the point source (emitter). The solution field was decomposed into amplitude and phase in the frequency domain. Amplitudes for simulation experiments: a) 1, b) 2 and c) 3. Because the source is defined on a single point, the quantities of the wave simulation are not physical and the solution field is not pressure. But an integration over a distribution of point sources using the derived formulae in section 5.2 will provide a solution field in terms of pressure and with the units of Pascal. Phases for simulation experiments: d) 1, e) 2 and f) 3. The phases were wrapped to $[-\pi, \pi]$ rad. The plots are not for the purpose of a direct comparison with the toolbox, but they show how modifying the toolbox to compute a point mass source (61), which is a discretisation of (59), will approximate the analytic action (57).

were much smaller than the Green's formula (green plot), they were enlarged by a factor 666.7 for a better visualisation (magenta plot). As shown in these figures, using all the chosen source pluses, the amplitudes computed using the modified k-Wave (red plot) match the analytically calculated amplitudes (green plot). In the same way, figures 7(d), 7(e) and 7(f) show the phases, which have been wrapped to $[-\pi, \pi]$ rad. As shown in these figures, the phases approximated by the modified k-Wave match the analytically calculated phases for all the receivers. It must be emphasized again that the purpose of this experiment was not a direct comparison with the toolbox, but it was explained how modifying the input given to the toolbox based on Eq. (61), which is a discretisation of (59), will approximate the analytic action (57).

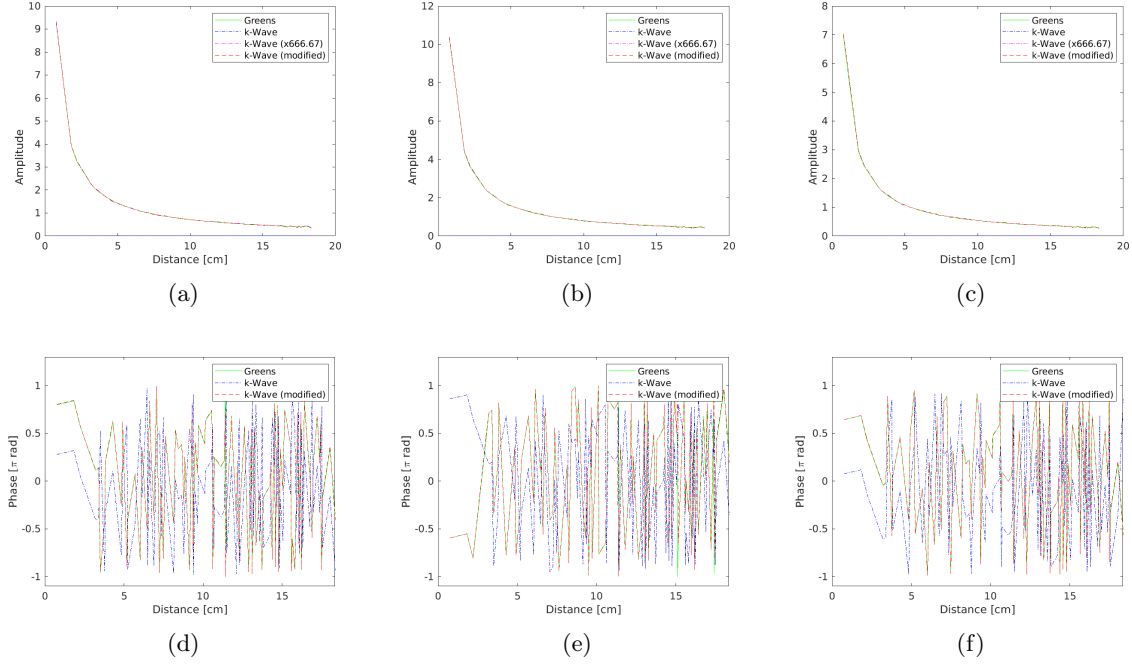


FIGURE 7. 3D medium. The solution field recorded on all the receivers after radiation of the point source (emitter). The solution field was decomposed into amplitude and phase in the frequency domain, and is shown at the single frequency $f_{\max}/2$ as a function of distances of the receivers to the emitter. Amplitudes for simulation experiments: a) 1, b) 2 and c) 3. Phases for simulation experiments: d) 1, e) 2 and f) 3. The phases were wrapped to $[-\pi, \pi]$ rad. The plots are not for the purpose of a direct comparison with the toolbox, but they show how modifying the toolbox to compute a point mass source (61), which is a discretisation of (59), will approximate the analytic action (57).

7. DISCUSSION

This manuscript explained step by step approaches for numerical approximations to analytic solutions to the wave equation. It was shown theoretically and numerically that the numerical approximations to the wave equation is equivalent to representing the wavefield solution as a superposition of actions of causal Green's functions on a volumetric or surface source over the space and time of support of the source. The author felt that this equivalence is important for accurately approximating forward and back-projected wavefields and its potential limitations, which may have not been paid due attention.

The primary formula (12) solves a causal variant of the wave equation (1) or its canonical form (2), and represents the propagated pressure wavefield p directly in terms of the radiation source s . This solution of the wave equation is commonly used in Geophysics and Biomedical studies, for example this solution was used in the developed ray-born inversion approaches for quantitative ultrasound tomography [71, 72]. For practical reasons, it may be more convenient to represent the wavefield in terms of a surface source. Correspondingly, the *Kirchhoff-Helmholtz* formula is used to represent the wavefield in terms of a source defined over a finite closed surface bounding the

radiation source s , and the *Rayleigh-Sommerfeld* formula was derived for a source mounted on a flat plane.

It was shown that modelling the mass source is the key step for accurate numerical approximations matching the derived analytic solutions to the wave equation. Correspondingly, a rigorous approach was proposed for modelling and including time-varying source in the wave equation for accurate numerical approximations of forward and back-projected fields. The k-Wave Version 1.3, was used, and the step for discretising the gradient of fields was kept unchanged, but the steps for including the mass source were modified based on the procedure explained in section 5. The proposed approach is based on applying triangulation on the space of the volumetric or surface source, and then mapping the space of the source onto the regular computational grid via a change of variable of a spatial integral formula derived from an associated boundary-value problem. Note that compared to the numerical integration approach in [73], section II. C, the triangulation step included in our proposed approach for modelling the mass source is more accurate, because it is not limited to a mesh with equidistant nodes, and will thus be more accurate near boundaries of the source.

It was shown that compared to analytical or ray-based methods, full-wave methods for solving the wave equation have a limitation for modelling doublet surface sources, because these kinds of sources are functions of normal derivative of the Green's function over the surface of the source and therefore depend on *obliquity factor* or its equivalent *solid angle*, the angle an elemental area on the surface bounding the source can be seen by any arbitrary point in the solution space. This limitation is more dominant for approximating *backprojection* or *time-reversal* fields, which are represented as solutions to an *Interior-field Kirchhoff-Helmholtz* integral for which a homogeneous *Dirichlet* condition is imposed over the measurement surface for an associated inward-directed causal Green's function.

The numerical approach proposed for including the time-varying source in the wave equation was validated via a comparison with an associated analytic solution. For the sake of simplicity and generality, this comparison was done for a source defined on a single point. The matches obtained between the analytical and numerical solutions to the wave equation are very important for future studies in the fields related to the biomedical acoustics.

8. CONCLUSION

This manuscript shared scientific experience of the author about how the step for inclusion of time-varying source in the wave equation should be treated for obtaining numerical solutions matching the common analytic solutions to the acoustic wave equation, to the best of the author's knowledge.

APPENDIX A. 3D GREEN'S FUNCTION

The time-domain Green's function can be expressed in the form of a Fourier integral. Accordingly, taking a spatio-temporal Fourier transform of the wave equation (4) gives $(k^2 - K^2)\tilde{G}(\mathbf{K}, \omega) = -1$, which is related to the time-domain Green's function using

$$g(\mathbf{x}_\partial, t_\partial) = \frac{-1}{(2\pi)^4} \int_{-\infty}^{\infty} d\omega \int d\mathbf{K} \frac{e^{i(\mathbf{K} \cdot \mathbf{x}_\partial - \omega t_\partial)}}{k^2 - K^2}, \quad (63)$$

where $g(\mathbf{x}_\partial, t_\partial) = 1/(2\pi) \int_{-\infty}^{\infty} d\omega G(\mathbf{x}_\partial, \omega) e^{-i\omega t_\partial}$ and $G(\mathbf{x}_\partial, \omega) = 1/(2\pi)^3 \int d\mathbf{K} \tilde{G}(\mathbf{K}, \omega) e^{i\mathbf{K} \cdot \mathbf{x}_\partial}$. For the latter, \mathbf{K} denotes the vector of spatial frequencies along the Cartesian coordinates. Here, the integrand has simple poles at $k = \pm K$. This integral does not uniquely define a Green's function. To obtain a unique solution, a causal Green's function, which vanishes at $t_\partial < 0$ and has homogeneous Cauchy conditions at $t_\partial = 0$, gives an integration contour that lies above both poles and is closed

over the lower half-plane semicircle [70]. Accordingly, a causal form of Eq. (63) can be written in the form

$$g_+(\mathbf{x}_\partial, t_\partial) = \frac{-c^2}{(2\pi)^4} \int d\mathbf{K} e^{i\mathbf{K} \cdot \mathbf{x}_\partial} \int_{\text{contour}} d\omega \frac{e^{-i\omega t_\partial}}{\omega^2 - c^2 K^2}, \quad t_\partial > 0. \quad (64)$$

Using Cauchy Residue Theorem, the so-called *Retarded* Green's function will be derived.

$$g_+(\mathbf{x}_\partial, t_\partial) = \frac{c}{(2\pi)^3} \int d\mathbf{K} e^{i\mathbf{K} \cdot \mathbf{x}_\partial} \frac{\sin(cK t_\partial)}{K}, \quad t_\partial > 0. \quad (65)$$

Now, transforming the variables of integration to a spherical polar coordinate with polar axis along \mathbf{x}_∂ , together with using a substitution $\mathbf{K} \cdot \mathbf{x}_\partial = K x_\partial \cos(\theta)$ with θ the polar angle of \mathbf{K} , give [70]

$$\begin{aligned} g_+(\mathbf{x}_\partial, t_\partial) &= \frac{c}{(2\pi)^2} \int_0^\infty dK K \sin(cK t_\partial) \int_0^\pi d\theta e^{iK x_\partial \cos(\theta)} \sin(\theta) \\ &= \frac{c}{(2\pi)^2 x_\partial} \int_{-\infty}^\infty dK \sin(cK t_\partial) \sin(K x_\partial), \quad t_\partial > 0. \end{aligned} \quad (66)$$

Finally, expanding sine functions using Euler's identity, and a replacement $\delta(\mathbf{x}) = 1/(2\pi)^3 \int d\mathbf{K} e^{i\mathbf{K} \cdot \mathbf{x}}$ gives the causal Green's function $g_+(\mathbf{x}_\partial, t_\partial) = 1/(4\pi x_\partial) \delta(t_\partial - x_\partial/c)$, $t_\partial > 0$, which is zero at $t_\partial < 0$.

APPENDIX B. SOMMERFELD RADIATION CONDITION

At large distances from the source, an approximate Green's function can be obtained using a *far-field* approximation

$$x_\partial = |\mathbf{x} - \mathbf{x}'| = (x^2 + x'^2 - 2\mathbf{x} \cdot \mathbf{x}')^{1/2} \approx x - \hat{\mathbf{x}} \cdot \mathbf{x}', \quad x \rightarrow \infty, \quad (67)$$

where $\hat{\mathbf{x}} = \mathbf{x}/x$ is a unit vector along \mathbf{x} . Plugging the approximation (67) into the outgoing Green's function (19), and substituting the resulting *far-field* approximated Green's function into Eq. (23), give the *Sommerfeld radiation condition* (SRC) [70]

$$p_+(\mathbf{x}, \omega) \approx f(\hat{\mathbf{x}}, \omega) \frac{e^{ikx}}{x}, \quad x \rightarrow \infty, \quad (68)$$

where

$$f(\hat{\mathbf{x}}, \omega) = \frac{1}{4\pi} \int_{\nu_s} d\mathbf{x} S(\mathbf{x}, \omega) e^{-ik\hat{\mathbf{x}} \cdot \mathbf{x}}. \quad (69)$$

Alternatively, the SRC can be expressed using

$$\lim_{x \rightarrow \infty} x^{\frac{d-1}{2}} \left[\frac{\partial}{\partial x} P_+(\mathbf{x}, \omega) - ik P_+(\mathbf{x}, \omega) \right] \rightarrow 0, \quad (70)$$

where we remind that $d \in \{2, 3\}$ stands for the number of dimensions. Eq. (70) can be derived directly from (68).

REFERENCES

- [1] T. D. Mast, L. P. Souriau, D. -L. D. Liu, M. Tabei, A. I. Nachman and R. C. Waag, "A k-space method for large-scale models of wave propagation in tissue", *IEEE Trans. Ultrason. Ferroelectr. Freq.*, vol. 48, no. 2, pp. 341-354, March 2001, doi: 10.1109/58.911717.
- [2] M. Tabei, T. D. Mast, and R. C. Waag, "A k-space method for coupled first-order acoustic propagation equations", *J. Acoust. Soc. Am.* vol. 111, pp. 53-63, 2002.
- [3] B. E. Treeby and B. T. Cox, "k-Wave: MATLAB toolbox for the simulation and reconstruction of photoacoustic wave fields", *J. Biomed. Opt.* vol. 15, no. 2, 021314, 2010.
- [4] S. Holm and S.P. N  sholm, "A causal and fractional all-frequency wave equation for lossy media", *The Journal of the Acoustical Society of America*, Vol. 130, no. 4, pp. 2195-2202, 2011.

- [5] B. Treeby and B. Cox, k-Wave user manual, “A Matlab toolbox for the time domain simulation of acoustic wave fields”, Version 1.1, 27th August 2016 (the last version).
- [6] M. J. Bencomo and W. W. Symes, “Discretization of multipole sources in a finite difference setting for wave propagation problems”, *Journal of Computational Physics*, vol. 386, pp. 296–322, 2019.
- [7] M. M. Cavalcanti, V. N. Domingos Cavalcanti, C. L. Frota and A. Vicente, “Stability for semilinear wave equation in an inhomogeneous medium with frictional localized damping and acoustic boundary conditions”, *SIAM J Control Optim.*, Vol. 58, no. 4, pp. 2411–2445, 2020.
- [8] A.A. Alcântara, B.A. Carmo, H.R. Clark, R. R. Guardia and M. A. Rincon, “Nonlinear wave equation with Dirichlet and Acoustic boundary conditions: theoretical analysis and numerical simulation”, *Comp. Appl. Math.* Vol. 41, no. 141, 2022, <https://doi.org/10.1007/s40314-022-01822-5>.
- [9] A. Siahkoobi, M. Louboutin and F. J. Herrmann, “The importance of transfer learning in seismic modeling and imaging”, *Geophysics*, Vol. 84, no. 6, pp. A47–A52, 2019, <https://doi.org/10.1190/geo2019-0056.1>.
- [10] A. Javaherian, F. Lucka and B. Cox, “Refraction-corrected ray-based inversion for three-dimensional ultrasound tomography of the breast”, *Inverse Problems*, vol. 36, no. 12, 125010, 2020.
- [11] Y. Tang, B. Sun and T. Alkhalifah, “Wave-equation migration velocity analysis via the optimal-transport-based objective function”, *Geophysics*, Vol. 87, no. 3, pp. U109–U120, 2022.
- [12] T. Furuya and R. Potthast, “Inverse medium scattering problems with Kalman filter techniques”, *Inverse Problems*, Vol. 38, no. 9, 095003, 2022.
- [13] S. Bhattacharyya, M. V. de Hoop, V. Katsnelson and G. Uhlmann, “Recovery of wave speeds and density of mass across a heterogeneous smooth interface from acoustic and elastic wave reflection operators”, *GEM-International Journal on Geomathematics*, Vol. 13, no. 1, 2022.
- [14] S. Holm, S. N. Chandrasekaran and S. P. Näsholm, “Adding a low frequency limit to fractional wave propagation models”, *Front.Phys.*, 11:1250742.2023.<https://doi.org/10.3389/fphy.2023.1250742>.
- [15] H. Chauris and M. Farshad, “Seismic differential semblance-oriented migration velocity analysis — Status and the way forward”, *Geophysics*, Vol. 88, no. 6, pp. U81–U100, 2023.
- [16] M. Bader, R. G. Clapp, K. T. Nihei, and B. Biondi, “Moment tensor inversion of perforation shots using distributed-acoustic sensing”, *Geophysics*, Vol. 88, no. 6, pp. 1–36, 2023. <https://doi.org/10.1190/geo2021-0661.1>.
- [17] M. Papadopolou, B. Brodic, E. Koivisto and A. Kaleshova, M. Savolainen, P. Marsden, and L. V. Socco, “High-resolution static corrections derived from surface-wave tomography: Application to mineral exploration”, *Geophysics*, Vol. 88, no. 6, B317–B328, 2023.
- [18] M. V. Eaid, S. D. Keating, K. A. Innanen, M. Macquet and D. Lawton, “Field assessment of elastic full-waveform inversion of combined accelerometer and distributed acoustic sensing data in a vertical seismic profile configuration”, *Geophysics*, vol. 88, no. 6, pp. WC163–WC180, 2023.
- [19] B. Kaltenbacher and W. Rundell, “On the simultaneous reconstruction of the nonlinearity coefficient and the sound speed in the Westervelt equation”, *Inverse Problems*, Vol. 39, no. 10, p. 105001, 2023, DOI 10.1088/1361-6420/acef2.
- [20] W. Wang, G. A. McMechan and J. Ma, “Reweighted variational full-waveform inversions”, *Geophysics*, Vol. 88, no. 4, R499–R512 <https://doi.org/10.1190/geo2021-0766.1>.
- [21] G. Uhlmann and Y. Zhang, “An inverse boundary value problem arising in nonlinear acoustics”, *SIAM Journal on Mathematical Analysis*, Vol. 55, no. 2, pp. 1364–1404, 2023.
- [22] B. Kaltenbacher and V. Nikolić, The vanishing relaxation time behavior of multi-term nonlocal Jordan–Moore–Gibson–Thompson equations, *Nonlinear Analysis: Real World Applications*, Vol. 76, pp. 103991, 2024, <https://doi.org/10.1016/j.nonrwa.2023.103991>.
- [23] J. Qian, P. Stefanov, G. Uhlmann and H. Zhao, “An Efficient Neumann series-based algorithm for thermoacoustic and photoacoustic tomography with variable sound speed”, *SIAM Journal on Imaging Sciences*, Vol. 4, no. 3, 2011. doi: 10.1137/100817280.
- [24] T. Tarvainen, B. T. Cox, J. Kaipio, and S. R. Arridge, “Reconstructing absorption and scattering distributions in quantitative photoacoustic tomography”, *Inverse Problems*, Vol. 28, 2012, p. 084009.
- [25] R. Kowar and O. Scherzer, “Attenuation Models in Photoacoustics”. In: H. Ammari (eds) *Mathematical Modeling in Biomedical Imaging II. Lecture Notes in Mathematics*, Vol. 2035, 2012. Springer, Berlin, Heidelberg. <https://doi.org/10.1007/978-3-642-22990-94>.
- [26] X. L. Dean-Ben, A. Buehler, V. Ntziachristos and D. Razansky, “Accurate model-based reconstruction algorithm for three-dimensional optoacoustic tomography”, *IEEE Transactions on Medical Imaging*, Vol. 31, no. 10, pp. 1922–1928, 2012.

- [27] A. Hauptmann et al., “Model-Based Learning for Accelerated, Limited-View 3-D Photoacoustic Tomography”, *IEEE Transactions on Medical Imaging*, vol. 37, no. 6, pp. 1382-1393, June 2018, doi: 10.1109/TMI.2018.2820382.
- [28] M.Haltmeier and L.V.Nguyen, “Analysis of iterative methods in photoacoustic tomography with variable sound speed”, *SIAM Journal on Imaging Sciences*, Vol.10,no.2,2017, doi: 10.1137/16M1104822.
- [29] J. A. Guggenheim, J. Li, T. J. Allen, R. J. Colchester, S. Noimark, O. Ogunlade, I. P. Parkin, I. Papakonstantinou, A. E. Desjardins, E. Z. Zhang and P. C. Beard, “Ultrasensitive plano-concave optical microresonators for ultrasound sensing”. *Nature Photon*, Vol. 11, pp. 714-719, 2017. <https://doi.org/10.1038/s41566-017-0027-x>.
- [30] A. Javaherian and S. Holman, “A continuous adjoint for photo-acoustic tomography of the brain”, *Inverse Problems*, vol. 34, no. 8, p. 085003, 2018.
- [31] A.Javaherian and S.Holman, “Direct quantitative photoacoustic tomography for realistic acoustic media”, *Inverse Problems*,vol.35,no.8,084004,2019.
- [32] S.Antholzer, M.Haltmeier and J.Schwab, “Deep-learning for photoacoustic tomography from sparse data”, *Inverse Problems in Science and Engineering*, Vol.27, no.7,pp.987-1005, 2019. doi: 10.1080/17415977.2018.1518444.
- [33] S. Guan, A. A. Khan, S. Sikdar and P. V. Chitnis, “Fully dense UNet for 2-D sparse photoacoustic tomography artifact removal”, *IEEE Journal of Biomedical and Health Informatics*, vol. 24, no. 2, pp. 568-576, Feb. 2020, doi: 10.1109/JBHI.2019.2912935.
- [34] S. Na and L. V. Wang, “Photoacoustic computed tomography for functional human brain imaging”, *Biomed. Opt. Express*, Vol. 12, pp. 4056-4083, 2021.
- [35] J. Grohl, M. Schellenberg, K. Dreher and L. Maier-Hein, “Deep learning for biomedical photoacoustic imaging: A review”, *Photoacoustics*, Vol. 22, 100241, 2021.
- [36] E. Park, S. Park, H. Lee, M. Kang, C. Kim and J. Kim, “Simultaneous dual-modal multispectral photoacoustic and ultrasound macroscopy for three-dimensional whole-body imaging of small animals”, *Photonics*, Vol. 8, pp. 13, 2021.
- [37] L. Nguyen, M. Haltmeier, R Kowar, and N. Do, “Analysis for full-field photoacoustic tomography with variable sound speed”, *SIAM Journal on Imaging Sciences*, Vol. 15, no. 3, 2022, 10.1137/21M1463409.
- [38] S. M. Ranjbaran, H. S. Aghamiry, A. Gholami, S. Operto and K. Avanaki, “Quantitative photoacoustic tomography using iteratively refined wavefield reconstruction inversion: a simulation study”, in *IEEE Transactions on Medical Imaging*, doi: 10.1109/TMI.2023.3324922.
- [39] B. M. Afkham, K. Knudsen, A. K. Rasmussen and T. Tarvainen, “A Bayesian approach for consistent reconstruction of inclusions”, <https://arxiv.org/abs/2308.13673>.
- [40] M. Suhonen, A. Pulkkinen, and T. Tarvainen, “Single-stage approach for estimating optical parameters in spectral quantitative photoacoustic tomography”, *J. Opt. Soc. Am.*, Vol. 41, no. 3, pp. 527-542, 2024.
- [41] H. Park, J. Yao and Y. Jing, “A frequency-domain model-based reconstruction method for transcranial photoacoustic imaging: A 2D numerical investigation”, *Photoacoustics*, Vol. 33, 2023, p. 100561.
- [42] N. Hänninen, A. Pulkkinen, S. Arridge and T. Tarvainen, “Estimating absorption and scattering in quantitative photoacoustic tomography with an adaptive Monte Carlo method for light transport”, *Inverse Problems and Imaging*, doi: 10.3934/ipi.2024006, 2024.
- [43] A. Hauptmann and T. Tarvainen, “Model-based reconstructions for quantitative imaging in photoacoustic tomography”, arXiv preprint, arXiv:2311.15735.
- [44] F. Li, U. Villa, N. Duric and M. A. Anastasio, “A Forward Model Incorporating Elevation-Focused Transducer Properties for 3-D Full-Waveform Inversion in Ultrasound Computed Tomography”, in *IEEE Transactions on Ultrasonics, Ferroelectrics, and Frequency Control*, vol. 70, no. 10, pp. 1339-1354, Oct. 2023, doi: 10.1109/TUFFC.2023.3313549.
- [45] G. Y. Sandhu, C. Li, O. Roy, S. Schmidt and N. Duric, Frequency domain ultrasound waveform tomography: breast imaging using a ring transducer, *Phys. Med. Biol.*, Vol. 60, 5381–5398, 2015.
- [46] A. V. Goncharsky and S. Y. Romanov, “Iterative methods for solving coefficient inverse problems of wave tomography in models with attenuation”, *Inverse Problems*, vol. 33, pp. 025003, 2017.
- [47] J. W. Wiskin, D. T. Borup, E. Iuanow, J. Klock and M. W. Lenox, “3-D Nonlinear Acoustic Inverse Scattering: Algorithm and Quantitative Results”, *IEEE T ULTRASON FERR*, vol. 64, no. 3, 2017.
- [48] H. S. Aghamiry, A. Gholami and Stéphane Operto, “Improving full-waveform inversion by wavefield reconstruction with the alternating direction method of multipliers”, *Geophysics*, Vol.84, no. 1, pp. R139–R162, 2019. doi: <https://doi.org/10.1190/geo2018-0093.1>.
- [49] L. Guasch, O. Calderón Agudo, M. Tang, P. Nachev, and M. Warner, “Full-waveform inversion imaging of the human brain”. *Nature Digital Medicine*, vol. 3, 28, 2020.

- [50] F. Faucher and O. Scherzer, Adjoint-state method for Hybridizable Discontinuous Galerkin discretization, application to the inverse acoustic wave problem, *Computer Methods in Applied Mechanics and Engineering*, Vol. 31 372, 2020.
- [51] F. Lucka, M. Perez-Liva, B. E. Treeby and B. T. Cox, “High resolution 3D ultrasonic breast imaging by time-domain full waveform inversion”, *Inverse Problems*, Vol. 38, 025008, 2022.
- [52] F. Li, U. Villa, S. Park and M. A. Anastasio, “3-D Stochastic Numerical Breast Phantoms for Enabling Virtual Imaging Trials of Ultrasound Computed Tomography”, in *IEEE Transactions on Ultrasonics, Ferroelectrics, and Frequency Control*, vol. 69, no. 1, pp. 135-146, Jan. 2022, doi: 10.1109/TUFFC.2021.3112544.
- [53] I. E. Ulrich, S. Noe, C. Boehm, N K Martiartu, B Lafci, X. L. Dean-Ben, D. Razansky and A.Fitchner, “Full-waveform inversion with resolution proxies for in-vivo ultrasound computed tomography”, 2023 IEEE International Ultrasonics Symposium (IUS), Montreal, QC, Canada, 2023, pp. 1-4, doi: 10.1109/IUS51837.2023.10308297.
- [54] L. Lozenski, H. Wang, F. Li, M. Anastasio, B. Wohlberg, Y. Lin, and U. Villa, “Learned Full Waveform Inversion Incorporating Task Information for Ultrasound Computed Tomography”, in *IEEE Transactions on Computational Imaging*, Vol. 10, pp. 69-82, 2024, doi: 10.1109/TCI.2024.3351529
- [55] D. Schweizer, R. Rau, C. D. Bezek, R. A. Kubik-Huch and O. Goksel, “Robust Imaging of Speed of Sound Using Virtual Source Transmission”, in *IEEE Transactions on Ultrasonics, Ferroelectrics, and Frequency Control*, Vol. 70, no. 10, pp. 1308-1318, 2023.
- [56] Z. Zeng, Y. Zheng, Y. Zheng, Y. Li, Z. Shi Aand H. Sun, “Neural Born series operator for biomedical ultrasound computed Tomography”, 2023, <https://arxiv.org/abs/2312.15575>.
- [57] S. Operto, A. Gholami, H. S. Aghamiry, G. Guo, S. Beller, K. Aghazade, F. Mamfoumbi, L. Combe and A. Ribodetti, “Extending the search space of full-waveform inversion beyond the single-scattering Born approximation: A tutorial review”, *Geophysics* 2023;; Vol. 88, no. 6, pp. R671–R702. doi: <https://doi.org/10.1190/geo2022-0758.1>.
- [58] M. Soleimani, T. Rymarczyk and G. Kłosowski, “Ultrasound Brain Tomography: Comparison of Deep Learning and Deterministic Methods”, in *IEEE Transactions on Instrumentation and Measurement*, Vol. 73, pp. 1-12, 2024, Art no. 4500812, doi: 10.1109/TIM.2023.3330229.
- [59] L. Borcea, J. Garnier, A. V. Mamonov and J. Zimmerling, “Waveform inversion with a data driven estimate of the internal wave”, *SIAM Journal on Imaging Sciences*, Vol. 16, no. 1, pp. 280-312, 2023, <https://doi.org/10.1137/22M1517342>.
- [60] S. Ziegler, T. Santos and J. L. Mueller, “Regularized full waveform inversion for low frequency ultrasound tomography with a structural similarity EIT prior”, *Inverse Problems and Imaging*, vol. 18, no. 1, pp. 86-103, 2024, doi:10.3934/ipi.2023023.
- [61] A. Pulkkinen, B. Werner, E. Martin and K. Hynynen, “Numerical simulations of clinical focused ultrasound functional neurosurgery”, *Physics in Medicine & Biology*, vol. 59, no. 7, p. 1679, 2014.
- [62] A. Kyriakou, E. Neufeld, and B. Werner, G. Székely and N. Kuster, “Full-wave acoustic and thermal modeling of transcranial ultrasound propagation and investigation of skull-induced aberration correction techniques: a feasibility study”. *J Ther Ultrasound*, Vol. 3, no. 11, 2015. <https://doi.org/10.1186/s40349-015-0032-9>.
- [63] J. K. Mueller, L. Ai, P. Bansal and W. Legon, “Numerical evaluation of the skull for human neuromodulation with transcranial focused ultrasound”, *J. Neural Eng.*, Vol. 14, p.066012 (19pp), 2017.
- [64] C. Pasquinelli, L.G. Hanson, H.R. Siebner, H.J. Lee and A. Thielscher, “Safety of Transcranial focused ultrasound stimulation: A systematic review of the state of knowledge from both human and animal studies”, *Brain Stimul.*, Vol. 12, no. 6, pp. 1367-1380, 2019. doi: 10.1016/j.brs.2019.07.024. Epub 2019 Jul 31. PMID: 31401074.
- [65] P. Gaur, K.M. Casey, J. Kubanek, N. Li, M. Mohammadjavadi, Y. Saenz, G.H. Glover, D.M. Bouley and K.B. Pauly. “Histologic safety of transcranial focused ultrasound neuromodulation and magnetic resonance acoustic radiation force imaging in rhesus macaques and sheep”. *Brain Stimul.* 2020 May-Jun;13(3):804-814. doi: 10.1016/j.brs.2020.02.017. Epub 2020 Feb 21. PMID: 32289711; PMCID: PMC7196031.
- [66] T. Bancel et al., “Comparison Between Ray-Tracing and Full-Wave Simulation for Transcranial Ultrasound Focusing on a Clinical System Using the Transfer Matrix Formalism”, in *IEEE Transactions on Ultrasonics, Ferroelectrics, and Frequency Control*, vol. 68, no. 7, pp. 2554-2565, July 2021, doi: 10.1109/TUFFC.2021.3063055.
- [67] J-F Aubry, O. Bates, C. Boehm, K. B. Pauly, D. Christensen, C. Cueto, P. G  lat, L. Guasch, J. Jaros, Y. Jing, R. Jones, N. Li, P. Marty, H. Montanaro, E. Neufeld, S. Pichardo, G. Pinton, A. Pulkkinen, A. Stanzola, A. Thielscher, B Treeby and E. Van’t Wout, “Benchmark problems for transcranial ultrasound simulation: Inter-comparison of compressional wave models”, *J. Acoust. Soc. Am.*, vol. 152, pp. 1003–1019, 2022.

- [68] J-F Aubry, D. Attali, M. Schafer, E. Fouragnan, C. Caskey, R. Chen, G. Darmani, E. J. Bubrick, J. Sallet, C. Butler, C. Stagg, M. Klein-Flugge, S-S Yoo, B. Treeby, L. Verhagen and K. B. Pauly, “ITRUSST Consensus on Biophysical Safety for Transcranial Ultrasonic Stimulation”, 2023, <https://arxiv.org/abs/2311.05359>.
- [69] M. Xu and L. V. Wang, “Universal back-projection algorithm for photoacoustic computed tomography”, *PHYSICAL REVIEW E*, Vol. 71, pp. 016706 (2005).
- [70] A.J. Devaney, “Mathematical Foundations of Imaging, Tomography and Wavefield Inversion”. Cambridge University Press; 2012.
- [71] A. Javaherian and B. Cox, “Ray-based inversion accounting for scattering for biomedical ultrasound tomography”, *Inverse Problems*, vol. 37, no.11, 115003, 2021.
- [72] A. Javaherian, “Hessian-inversion-free ray-born inversion for high-resolution quantitative ultrasound tomography”, 2023, <https://arxiv.org/abs/2211.00316>.
- [73] E. S. Wise, B. T. Cox, J. Jaros and B. E. Treeby, “Representing arbitrary acoustic source and sensor distributions in Fourier collocation methods”, *J. Acoust. Soc. of Am.*, vol. 146, no. 1, pp. 278-288, 2019.
- [74] M Dantuma et al, “Fully three-dimensional sound speed-corrected multi-wavelength photoacoustic breast tomography”, 2023, <https://arxiv.org/abs/2308.06754>.